# COHERENT DYNAMICS IN NETWORKS OF SOFT-THRESHOLD INTEGRATE-AND-FIRE NEURONS ON THE RING

LAUREN FORBES\*, JARED GROSSMAN\*, MONTIE AVERY\*, RYAN GOH\*, AND GABRIEL KOCH OCKER\* $^{\dagger}$ 

Abstract. We study bifurcations in networks of integrate-and-fire neurons with stochastic spike emission, focusing on the effects of the spatial and temporal structure of the synaptic interactions. Using a deterministic mean-field approximation of the population dynamics, we characterize spatial, temporal, and spatiotemporal patterns of macroscopic activity. In the mean-field theory, synaptic delays give rise to uniform oscillations across the population through a subcritical Hopf bifurcation of the stationary uniform equilibrium. With local excitation and long-range inhibition the network undergoes a Turing bifurcation, resulting in a localized area of sustained activity, or stationary bump. When the coupling has both delays, local inhibition, and long range excitation, the network undergoes a Turing-Hopf bifurcation leading to spatiotemporal dynamics, such as standing and traveling waves. When multiple instabilities are excited, we observe other complex spatiotemporal dynamics. We confirm all these predictions of the mean-field theory in simulations of the underlying stochastic model.

Relevance to Life Sciences. Spatiotemporal neural activity patterns are key features of sensory perception, decision-making, and working memory. These patterns depend on both the structure of synaptic connectivity and the intrinsic dynamics of neurons and synapses. Here, we study spatiotemporal dynamics in a simple spiking neuron model: soft-threshold integrate-and-fire networks. We show how the single-neuron and synaptic dynamics, together with the spatial structure of the network, determine the presence of various activity patterns. The synaptic structure we consider here incorporates transmission delays and spatially organized excitation-inhibition. In contrast to classic neural field theories, ours is derived from a specific microscopic neuron model whose parameters can be measured experimentally. We thus develop a method that can expose how specific neural and synaptic biophysics shape macroscopic activity patterns.

Mathematical Content. We extend a recent mean-field theory, for integrate-and-fire networks with stochastic spike emission, to incorporate temporally delayed and spatially nonlocal interactions. The resulting neural field equation resembles the classic Amari-Grossberg model, with an additional term from the reset of the membrane voltage following the emission of an action potential. We identify spatial, temporal, and spatiotemporal primary instabilities of the system. We numerically continue both temporally and spatially periodic solutions of the mean-field model and track their spectral stability to identify folds of finite-amplitude oscillations, as well as codimension-2 bifurcation points. This framework also exposes regimes of complex spatiotemporal dynamics, far from the onset of instabilities.

Key words. mean-field theory, neural field theory, oscillations, patterns

MSC codes. 92B20, 92C20, 35Q70, 35Q92, 35B36, 60G55

1. Introduction. Spatially and temporally patterned behavior in large-scale neuronal activity are thought to play a role in a wide range of neurobiological phenomena. Some examples include geometric visual hallucinations [22], orientation tuning in the visual cortex [4], and short term working memory [11, 12]. These spatiotemporal dynamics are often understood using neural field equations, which are macroscopic descriptions of large networks' activity [54, 2, 5, 27, 28]. Although they have proven extremely useful in modeling neuronal dynamics, these macroscopic equations lack biophysical detail and can fail to capture spatiotemporal behaviors observed in microscopic spiking network models [10]. The lack of a direct connection between scales obscures the relation between single-cell and population dynamics.

Integrate-and-fire (IF) models can capture a range of single-cell neural dynamics [48, 34, 37]. In these models, the nonlinear dynamics of spiking are replaced with a

<sup>\*</sup>Boston University, Department of Mathematics and Statistics (lcforbes@bu.edu, rgoh@bu.edu)
†and Center for Systems Neuroscience (gkocker@bu.edu).

simple fire-and-reset rule where the membrane voltage returns to a fixed value after the neuron emits a spike. IF models can be lower dimensional approximations of more bio-physical conductance based models such as the Hodgkin-Huxley model [1]. Networks of IF neurons can exhibit spatial, temporal and spatiotemporal patterns. Oscillations can be induced by either synaptic delays or excitatory-inhibitory interactions [8, 7, 51, 53]. The spatial profile of synaptic projections controls transitions between spatially incoherent and coherent activity [35, 43]. Despite their simple single neuron dynamics, large networks of IF neurons are high dimensional and complex. Therefore, to analytically study temporal and spatial transitions in the network-level dynamics, there has been much interest in field theories that are both analytically tractable and directly connected to the microscopic single-neuron properties [10, 46, 36].

Here, we study soft-threshold leaky IF (sLIF) networks, which incorporates stochastic spike emission and a leak term driving the membrane potential toward a resting value, alongside a corresponding mean-field theory [38]. In particular, we explore oscillatory, spatial, and spatiotemporal instabilities in networks of sLIF neurons with temporal or spatial structure in their synaptic interactions. First, we introduce the sLIF network and mean-field approximation (Section 2) and determine the linearized dispersion relation to identify various instabilities present in the model (Section 3.1). These instabilities, along with bifurcations of the resulting patterns, delineate regions in the parameter space phase diagram where there exist one or more qualitatively distinct steady state solutions of the model. Each of these steady states correspond to a different type of behavior exhibited by the network.

We identify ten distinct regions of parameter space (labeled (i)-(x)) where the network can support one or more activity states. Identifying the existence regions provides a qualitative picture of the dependence of the network dynamics on the spatiotemporal structure of synaptic connectivity. We identify and analyze four primary types of solutions: (a) homogeneous steady states, constant in both time and space, which correspond to either globally active or quiescent network states depending on whether activity is above or below threshold (Sections 3.1-3.2), (b) homogeneous oscillatory states, which correspond to global oscillations in network activity (Section 3.3), (c) stationary spatial patterns, in which only a portion of the profile is above threshold, corresponding to local activity in the network (Section 3.4), and (d) spatiotemporal patterns, including standing waves, traveling waves, and oscillating bumps (Section 3.5). Finally, we discuss the influence of more complex temporal coupling structures on the emergence of instabilities (Section 4). Together, our findings reveal how different structures of connectivity and temporal dynamics give rise to a rich repertoire of network behaviors in a spatially extended sLIF network. In particular we show that transmission delays and spatially structured excitation-inhibition in the synaptic connections support multiple kinds of activity states across different network structures, as well as multi-stability within individual structures.

2. The model. We will use a soft-threshold leaky integrate-and-fire neuron (sLIF) as our microscopic model to describe how individual neurons integrate incoming signals and generate action potentials (or spikes). We consider a network of N sLIF neurons on the ring  $[-\pi,\pi)$  (Fig. 1A). One-dimensional networks defined on periodic domains have been used to model feature selectivity in neuronal populations—for example, the sensitivity of neurons in the visual cortex to the orientation of visual stimuli [29, 4]. Neuron i has membrane voltage  $v_i(t)$  at time t. Let  $n_j(t)$  be the counting process associated with neuron j, recording the total number of spikes that neuron j has emitted up until time t. The increments of that process are  $dn_i(t)$ . After

neuron j emits a spike, its membrane potential is reset to the fixed value r. A postsynaptic neuron i receives and integrates spikes from presynaptic neuron j through the synaptic filter  $J_{ij}(s-D)$ , where s is the time since the presynaptic spike and D the synaptic delay (Fig. 1B).

We implement stochastic spike emission to model the variability in the membrane potentials at which neurons emit a spike [25]. This soft-threshold for spike emission distinguishes the sLIF model from classic LIF models, where neurons deterministically emit a spike at threshold. The increments  $dn_i(t)$  define a point process,  $\dot{n}_i(t)$ , called the spike train. We take its intensity to be  $f(v_i(t))$ , where f is a non-negative function. The intensity function is often chosen to be zero or near-zero below a threshold, so there is no or low chance of emitting a spike at low membrane voltages. Above threshold, f is increasingly higher so there is an increasing chance of generating a spike at higher voltages.

Finally, each neuron has resting potential  $E_i$ , also incorporating any external input currents. Together, the membrane voltage of neuron  $i, v_i(t)$ , evolves according to the Itô stochastic differential equation

$$dv_i(t) = \frac{dt}{\tau} \left( -v_i(t) + E_i + \frac{1}{N} \sum_{j=1}^{N} \int J_{ij}(t - s - D) \, dn_j(s) \right) - dn_i(t^+) \left( v_i(t) - r \right)$$

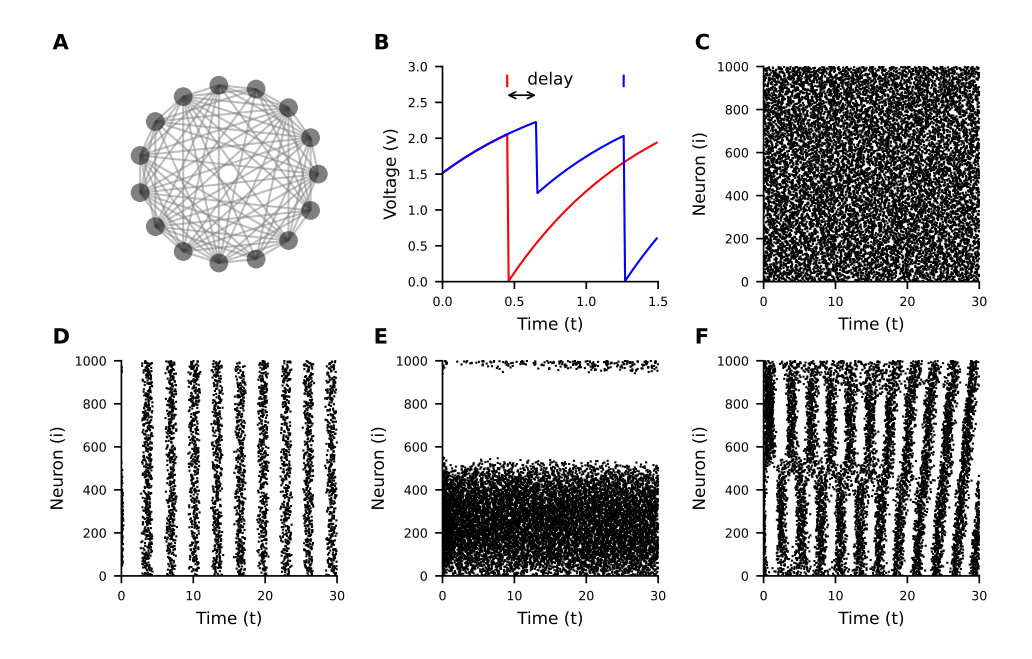


Fig. 1. The sLIF network (2.1) with coupling (3.4)-(3.6):  $J(x,t-D) = \frac{1}{2\pi}\delta(t-D)(J_0 + t)$  $J_1\cos(x)$  and D=1, E=2, and N=1000. A) A connected network on the ring. B) The delayed impact of a spike from a presynaptic neuron (red) on a postsynaptic neuron (blue). Spike times are marked with tick marks above.  $J_0 = -1$ . C) Homogeneous steady activity,  $J_0 = -2$ ,  $J_1 = 0$ . D) Homogeneous oscillatory activity,  $J_0 = -15$ ,  $J_1 = 0$ . E) Local activity,  $J_0 = -2$ ,  $J_1 = 20$ . F) A standing wave transitioning into a traveling wave,  $J_0 = -2$ ,  $J_1 = -20$ .

The neuron integrates input spikes from the rest of the network through the synaptic filter, or coupling function,  $J_{ij}(s)$ . With simple pulse coupling and no synaptic delay,  $J(x,t) = J_0\delta(t)$ , the sLIF network can exhibit homogeneous spiking behavior (Fig. 1C). When J(x,t) has more temporal and spatial structure, the network exhibits spatiotemporal dynamics. For non-zero delay values, the sLIF network can exhibit homogeneous oscillatory activity (Fig. 1D). Additionally, with sufficiently strong spatial modulation in J, the sLIF network exhibits spatially localized activity (Fig. 1E). Finally, if our coupling function has both delays and spatial modulation, the network can exhibit spatiotemporal dynamics with patterns of traveling or standing waves (Fig. 1F, which also shows a spontaneous, noise-induced transition between those two patterns). To understand these dynamics, we develop a neural field approximation of (2.1).

**2.1. Mean-field theory.** We will study a mean-field theory for (2.1), (2.2)

$$\partial_t \bar{v}(x,t) = -\bar{v}(x,t) + E + \int_{-\infty}^{t-D} \int_{-\pi}^{\pi} J(x-y,t-s-D) \,\bar{f}(y,s) \,dy \,ds \,-\bar{f}(x,t) \,\bar{v}(x,t)$$

Here,  $\bar{v}(x,t)$  is the mean membrane potential on the ring  $x \in [-\pi,\pi)$ ,  $\bar{f} := f(\bar{v})$  is the mean-field approximation of the spike trains  $\dot{n}$ ,  $J \in L^1([\pi,\pi) \times \mathbb{R}_+)$  is the synaptic filter, and E is the mean resting potential. We have non-dimensionalized the model by measuring time relative to  $\tau$  and the membrane potential relative to r, setting  $\tau = 1$  and r = 0. The presence of the reset term  $-\bar{f}(x,t)\bar{v}(x,t)$  differentiates this model from the classic Amari-Grossberg activity equations [2, 28].

The neural field theory (2.2) can be derived from the microscopic model (2.1) in two steps. We first take the mean-field limit of a large network,  $N \to \infty$ . This yields a stochastic PDE. We then make a purely deterministic mean-field approximation of that stochastic PDE.

We briefly and informally discuss two ways of taking the limit  $N \to \infty$ , both of which yield the mean-field approximation (2.2). In the first case, the connectivity  $J_{ij}(s)$  is a deterministic  $C^0$  function of the distance between neurons i and j (for fixed s). We place each neuron at  $x_i = -\pi + \frac{2\pi}{N}i$ , so that  $J_{ij}(s) = J(|x_i - x_j|, s)$ . In (2.1), the sum over neurons converges to a Riemann integral, yielding the stochastic partial integrodifferential equation

(2.3) 
$$\partial_t v(x,t) = -v(x,t) + E + (J * \dot{n})(x,t) - \dot{n}(x,t^+)v(x,t),$$

where \* is the convolution in both time and space and  $\dot{n}(x,t)$  is the spatiotemporal point process defined by the intensity f(v(x,t)).

In models with random (for example, randomly sparse) connectivity,  $J_{ij}(s)$  may not converge to a function of the position difference J(y,s). We instead take an approach that yields the statistics of  $J_{ij}(s)$  as functions of the position difference. We divide the ring into M segments, each containing m neurons so that N = Mm. We take the statistics of the connectivity between neurons i and j to depend only the distance  $|x_{\alpha}(i) - x_{\beta}(j)|$ , where  $\alpha(i)$  and  $\beta(j)$  are the segments containing neurons i and j. The synaptic current onto neuron i at time t is

$$\frac{1}{N} \sum_{j=1}^{N} \int J_{ij}(s-D) \, dn_j(t-s) = \frac{1}{M} \sum_{\beta=1}^{M} \frac{1}{m} \sum_{k=1}^{m} \int J_{\alpha(i)\beta}(s-D) \, dn_{(\beta-1)m+k}(t-s)$$

The inner sum concentrates around a joint second moment as  $m \to \infty$ . We assume that moment factorizes and take the limit  $M \to \infty$  so that

$$(2.4) \partial_t v(x,t) = -v(x,t) + E + (\langle J \rangle * \langle \dot{n} \rangle)(x,t) - \dot{n}(x,t^+)v(x,t),$$

where  $\langle J \rangle(y,s)$  is the mean strength of connections between two locations and  $\langle \dot{n} \rangle(x,t)$  the population mean activity of neurons at position x. The mean-field theory (2.2) was developed in this way in [38], for non-spatial networks, by constructing the joint density functional of the membrane voltages and spike trains using the response variable path integral formalism, reviewed in [13]. (2.2) can also be derived directly by averaging either (2.3) or (2.4) and truncating second and higher-order cumulants; (2.2) is the lowest-order truncation of both of their moment hierarchies. Fluctuation corrections to (2.2) will, however, differ depending on which large-network limit was taken [9, 6]. For further discussion of spatial mean-field limits of integrate-and-fire networks, see e.g., [33].

- **3. Results.** We begin our study of the dynamics of (2.2) by characterizing its homogenous equilibria and their stability. Throughout, we will take a rectified linear intensity function,  $f(v) = \lfloor v 1 \rfloor_+$ .
- **3.1. Homogeneous equilibria and dispersion relation.** There are three possible homogeneous equilibria of (2.2): one quiescent state below threshold  $(v_Q)$  and two solutions above threshold  $(v_{\pm})$ . These are given by (3.1)

$$v_0 = \begin{cases} v_Q = E & \text{if } E < 1, \\ v_+ = \left(J_0 + \sqrt{J_0^2 + 4(E - J_0)}\right)/2 & \text{if } J_0 > 2 + 2\sqrt{1 - E} \text{ or } J < 2, E > 1, \\ v_- = \left(J_0 - \sqrt{J_0^2 + 4(E - J_0)}\right)/2 & \text{if } J_0 > 2 + 2\sqrt{1 - E} \text{ and } J_0 > 2, E < 1, \end{cases}$$

where 
$$J_0 = \int \int J(x-y,t-s) ds dy$$
.

The quiescent state  $v_Q$  is always stable because when the voltage is below threshold the convolution and reset terms of (2.2) are zero, and the voltage converges to the resting potential E. In absence of delay and spatial modulation in the coupling,  $v_+(v_-)$  is always stable(unstable). Therefore, without spatial or temporal structure in the coupling, the mean activity will converge to  $v_+$  or  $v_Q$  [38]. The first three regions we identify in the phase diagram (Fig. 2A), where the stable homogeneous steady states exist, are:

- i) Q: Only a quiescent state  $(v_Q, \text{ below threshold})$  exists and is stable.
- ii) H: Only a high activity state  $(v_+, above threshold)$  exists and is stable.
- iii) Q-H: Both the quiescent and high activity states are stable.

In the bistable region Q-H, the unstable equilibrium  $v_{-}$  also exists and is the separatrix between the two stable solutions  $v_{Q}$  and  $v_{+}$ . The boundaries of Q-H are saddle node bifurcations, discussed further in Section 3.2.

To identify the instabilities of a homogeneous state  $v_0$ , we perform a standard linear stability analysis of the mean-field approximation (2.2). This yields a dispersion relation exposing the stability of  $v_0$  with respect to perturbations in each spatial Fourier mode. Given the threshold-linear intensity function,  $v_0$  above threshold ( $v_0 > 1$ ), and recalling the delay D in the synaptic coupling, the linearization of (2.2) about  $v_0$  is

(3.2) 
$$\partial_t w(x,t) = -2v_0 w(x,t) + \int_{-\infty}^{t-D} \int_{-\pi}^{\pi} J(x-y,t-s-D) w(y,s) \, dy \, ds$$

By taking the spatial Fourier transform of (3.2)  $\left(w(x,t)=\sum_{k\in\mathbb{Z}}\hat{w}_k(t)e^{ikx}\right)$  and mak-

ing the ansatz  $\hat{w}_k(t) = e^{\lambda_k t}$ , we obtain the dispersion relation

(3.3) 
$$\lambda_k = -2v_0 + e^{-\lambda_k D} \int_0^\infty \hat{J}_k(s) e^{-\lambda_k s} ds, \ k \in \mathbb{Z}$$

where  $\lambda_k$  is the eigenvalue associated with the  $k^{th}$  mode,  $\hat{w}_k$ . Note the dependence of the stability on the structure of interactions between the neurons since  $\hat{J}_k(t) = \int e^{-ikx} J(x,t) dx$  are the time-dependent  $k^{th}$  Fourier coefficients of the coupling function. See Appendix 6.3 for the dispersion relation for a general intensity function.

For simplicity, we assume delayed pulse coupling for the temporal profile and cosine coupling for the spatial profile:

(3.4) 
$$J(x, t - D) = J_{\text{space}}(x) J_{\text{time}}(t - D),$$

$$(3.5) J_{\text{time}}(t-D) = \delta(t-D),$$

(3.6) 
$$J_{\text{space}}(x) = \frac{1}{2\pi} (J_0 + J_1 \cos(x)).$$

With delayed pulse coupling, the dispersion relation (3.3) simplifies to

$$(3.7) \lambda_k = -2v_0 + \hat{J}_k e^{-\lambda_k D},$$

where  $\hat{J}_k$  is the  $k^{th}$  Fourier coefficient of the spatial coupling. For cosine coupling (3.6), there are only three nonzero Fourier coefficients,  $\hat{J}_0 = J_0$  and  $\hat{J}_{\pm 1} = J_1/2$ . Therefore, all spatial modes of the homogeneous equilibria other than k = 0 and k = 1 are always stable.

Other  $L^2$  spatial kernel functions can be studied in a similar way by using their Fourier coefficients in (3.3). For other choices of temporal kernels, the temporal integral in (3.3) will differ. In Section 4, we discuss two other temporal kernels which model the rise and fall times of the action potential in addition to the delay.

The dispersion relation (3.7) only pertains to equilibria above threshold. The quiescent state below threshold  $(v_Q)$  is always stable. Consequently, we restrict our analysis of instabilities to the two steady states above threshold  $(v_{\pm})$ . The location of primary instabilities are given by the dispersion relation (3.7) when  $\text{Re}(\lambda_k) = 0$  for different modes k and temporal frequencies  $\text{Im}(\lambda_k)$ .

These instabilities correspond to four smooth bifurcations of  $v_0$ : a saddle-node bifurcation (Section 3.2), a Hopf bifurcation (Section 3.3), a Turing bifurcation (Section 3.4), and a Turing-Hopf bifurcation (Section 3.5). At threshold ( $v_0 = 1$ ), non-smooth bifurcations can occur due to the non-smooth point of the intensity function f at its threshold. These are not described by the linearized analysis. We will study these numerically.

**3.2.** Homogeneous, static instabilities. The first instability of the homogeneous state is of the spatially-constant mode (k=0) with zero temporal frequency  $(\text{Im}(\lambda_0)=0)$ . With these assumptions and the instability condition  $(\text{Re}(\lambda_0)=0)$ , the dispersion relation (3.7) gives the location of the saddle-node bifurcation where  $v_{\pm}$  collide and vanish,

$$(3.8) J_0 = 2 + 2\sqrt{1 - E}.$$

Beyond the bifurcation, at lower  $J_0$  values, solutions tend toward the quiescent state  $v_Q$ . The bifurcation only occurs for  $J_0 > 2$  and E < 1 and does not depend on

the delay or spatial modulation in the coupling. The saddle-node curve forms the boundary between the bistable regime (Q-H) and the quiescent regime (Q) (Fig. 2A).

There is also a non-smooth saddle-node bifurcation at E=1 where  $v_-$  and  $v_Q$  collide and vanish. This bifurcation cannot be identified via the dispersion relation which is derived from the linearized dynamics above threshold. The non-smooth saddle-node curve is the boundary between the bistable region (Q-H) and high activity region (H) (Fig. 2A). These bifurcations were identified in [38]. If the intensity function f(v) is not threshold-linear, another saddle-node bifurcation between high and low activity states can emerge [40].

**3.3.** Delay-induced instability. Transmission delays can induce a Hopf bifurcation, at which homogeneous oscillations (sometimes also called bulk oscillations) of the network emerge. This oscillatory instability is in the spatially-constant mode (k=0) with nonzero frequency (Im $(\lambda_0) \neq 0$ ), occurring when a pair of complex conjugate eigenvalues cross the imaginary axis (Re $(\lambda_0) = 0$ ). From the dispersion relation (3.7), we find that  $v_+$  undergoes a Hopf bifurcation when

(3.9) 
$$\frac{-1}{D}\cos^{-1}\left(\frac{2v_{+}}{J_{0}}\right) = J_{0}\sqrt{1 - \left(\frac{2v_{+}}{J_{0}}\right)^{2}}$$

and  $v_+ > 1$ ,  $3J_0^2 + 4J_0 > 4E$ , D > 0, and  $J_0 < 0$ . See Appendix 6.4 for the derivation of (3.9). Beyond the Hopf bifurcation at lower  $J_0$  values, there are homogeneous oscillatory solutions  $v_{osc}(\text{Fig. 2B, upper})$ . As the delay is increased, the Hopf curve increases in  $J_0$  and approaches the curve  $3J_0^2 + 4J_0 = 4E$  (Fig. 2C), which is the boundary of the region on which the Hopf curve (3.9) is well-defined. Thus to obtain uniform oscillatory behavior in our network, the coupling must be delayed and sufficiently inhibitory with the reversal potential E above threshold. However, if E is too large, it offsets the inhibition and oscillations do not occur.

We find through numerical continuation of  $v_{osc}$  that the Hopf bifurcation (3.9) is subcritical as  $J_0$  and E decrease and D increases, with a branch of unstable oscillations emerging backwards out of the bifurcation point (Fig. 2D-F). See Appendix 6.2 for details of numerical continuation. Shortly after the minimum voltage on this unstable branch falls below threshold, it meets a stable branch through a fold of large amplitude limit cycles. The Hopf bifurcation and the fold of limit cycles bound a narrow bistable region of both  $v_+$  and  $v_{osc}$  (Fig. 2A, "O-H": dotted line). Decreasing E and E and E and period (Fig. 2J-L). Only in the parameter E does the oscillation amplitude later decrease until vanishing at a supercritical non-smooth Hopf bifurcation at E = 1, where E drops below threshold (Fig. 2E).

To summarize, we have found with the presence of delays, there are two additional regions of the phase diagram (Fig. 2A) involving  $v_{osc}$ :

- iv) O: Only a homogeneous, large-amplitude oscillation  $(v_{osc})$  around  $v_+$  is stable.
- v) O-H: Both a homogeneous oscillation  $(v_{osc})$  and high activity  $(v_+)$  state are stable.

The Hopf curve (3.9) is the boundary between the oscillatory (O) and bistable (O-H) regions, while the nearby fold of limit cycles is the boundary between the bistable (O-H) and high (H) activity regions. The non-smooth supercritical Hopf bifurcation at E=1 separates the oscillatory (O) and quiescent (Q) regions.

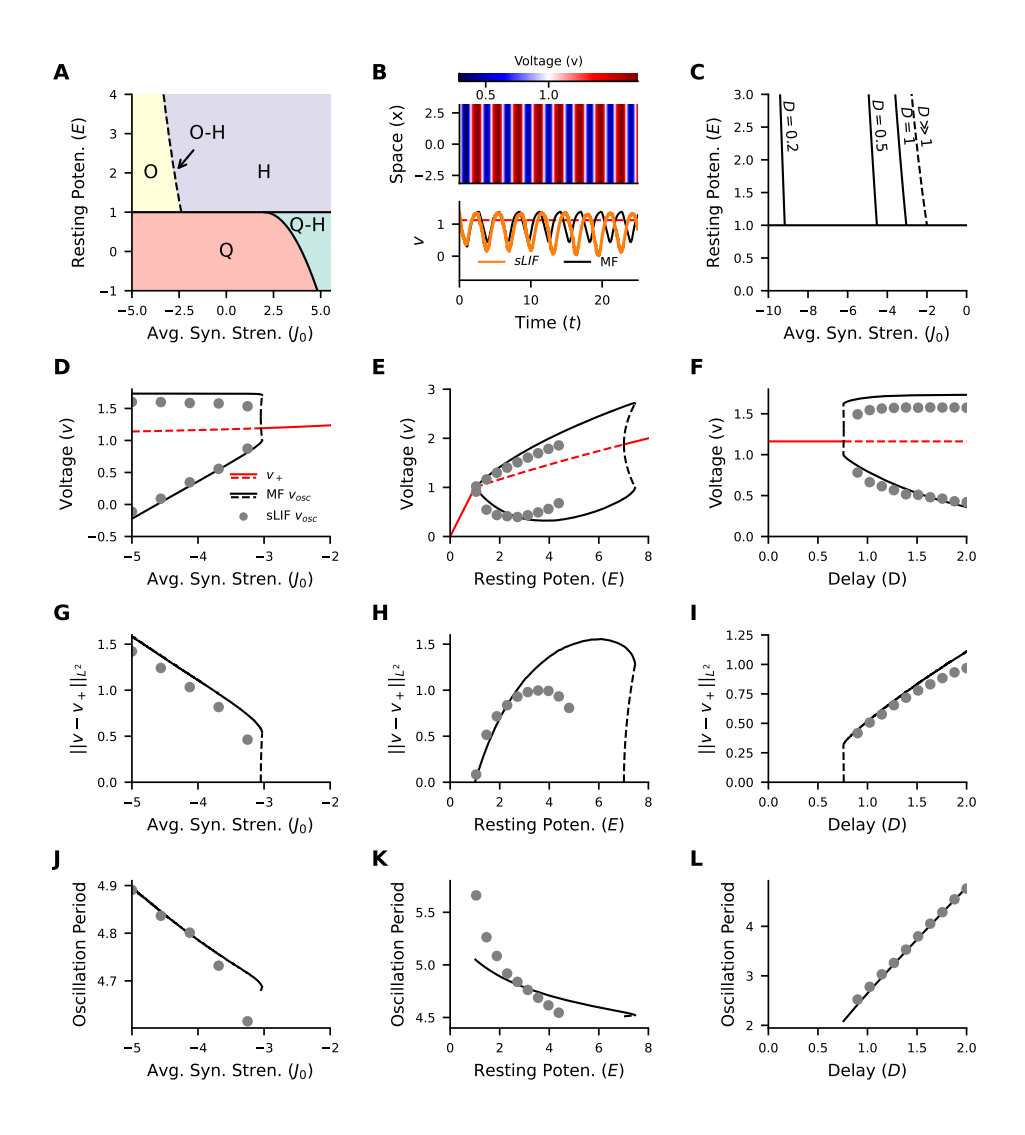


FIG. 2. Homogeneous oscillations in the mean-field approximation (2.2) and the sLIF Network (2.1) with delayed pulse coupling (3.5). Unless otherwise stated, parameters are  $J_0 = -4$ ,  $J_1 = 0$ , E = 3, and D = 2. A) Phase diagram of the mean-field approximation (2.2) in the  $J_0$ , E plane. Quiescent activity(Q, red), high activity (H, purple), bistable region of quiescent and high activity (Q-H, green), oscillatory (Q-H, green), oscillatory (Q-H, looper: homogeneous oscillation in mean-field approximation. Lower: The comparison of the population averages of both the above mean-field (black) and the sLIF network (orange) simulated at the same parameters C) Hopf curves (3.9) in the  $J_0$ , E plane with  $D = \{0.2, 0.5, 1\}$ . The dashed line shows the location of the Hopf curve as  $D \to \infty$ . D-F) Bifurcation diagrams in  $J_0$ , E, and D respectively, showing min/max amplitudes of stable (unstable) limit cycle with solid (dashed) black line and homogeneous solution (red). sLIF simulation data shown with grey circles. G-I)  $||v-v_+||_{L^2(0,P)}$  where v is the steady state oscillations and P is the oscillation period, shown for varying  $J_0$ , E, and D respectively. J-L) The period of the steady state oscillation for varying  $J_0$ , E, and D respectively.

Oscillatory behavior in the sLIF network (Fig. 2B lower panel, orange) qualitatively matches the mean-field approximation (Fig. 2B lower panel, black). Some discrepancy is expected due to the mean-field approximation. The maximum amplitude (Fig. 2D-F) and  $L^2$  norm (Fig. 2G-I) of the sLIF network oscillations (grey circles) is in general lower than that of the mean-field approximation (solid black line). Additionally, the oscillatory region of the sLIF network is smaller since the onset of oscillation at the Hopf bifurcation occurs at a lower E value, while the non-smooth Hopf bifurcation remains at threshold (Fig. 2E).

We are able to observe the small bistable region O-H in the sLIF network with a slow ramp of the bifurcation parameter through the region, starting on either side. We show this process first with the mean-field approximation, where we know the location of the Hopf bifurcation analytically and the location of the fold of limit cycles from numerical continuation. We then repeat the process using the sLIF network and observe similar phenomena.

We initialize a simulation of the mean-field (Fig. 3A, grey) in the oscillatory region (O) at a stable limit cycle and slowly increase the parameter  $J_0$ , through the bistable region (Fig. 3A, green). As the ramp continues, the limit cycle (Fig. 3B, Fig. 3A blue) persists until it loses stability at the fold marking the end of bistable region. The network activity then transitions to the stable homogeneous state and the oscillation decays.

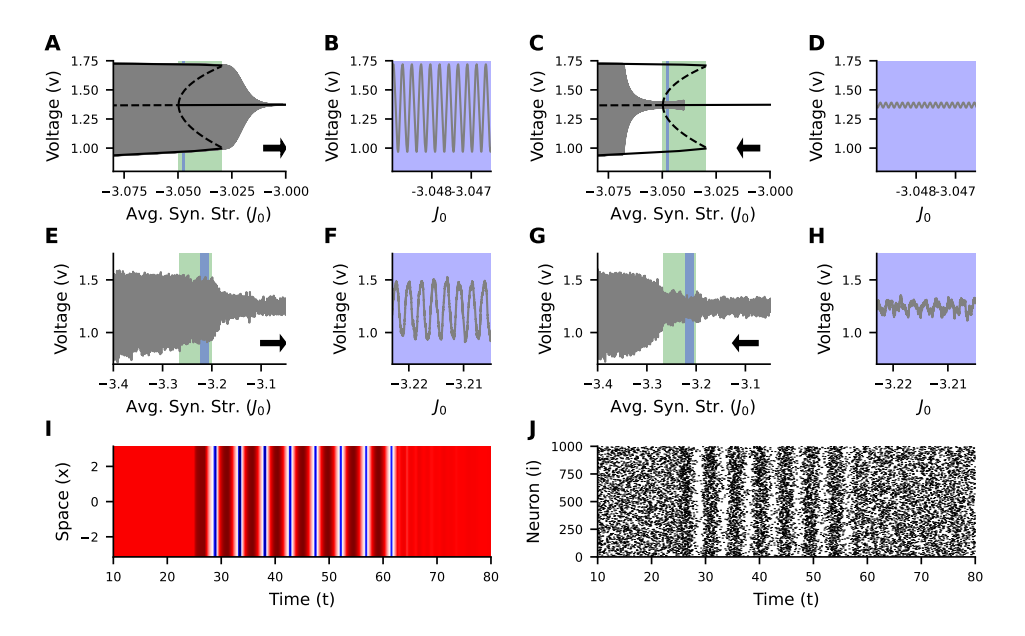
For the reverse ramp (Fig. 3C), we choose initial conditions above the bistable region near the stable homogeneous state. As  $J_0$  is slowly decreased through the bistable region, the network stays close to the stable homogeneous solution (Fig. 3D), until it loses stability at the Hopf bifurcation. A temporal oscillation then begins to grow and converges to the stable limit cycle. The delayed loss of stability, where the system stays close to the unstable homogeneous state after the bifurcation point, is expected when simulating smooth dynamical systems near a Hopf bifurcation [32]. It is due to the time it takes for the system to diverge from the unstable equilibrium.

We repeat both parameter ramps with the sLIF network. When increasing  $J_0$  from the oscillatory region (Fig. 3E), we observe a stable oscillation persisting in the bistable region (Fig. 3F) and a similar loss of stability of the limit cycle, but at a slightly lower  $J_0$  value than that of the mean-field approximation. Decreasing  $J_0$  from the homogeneous regime, we again observe similar behavior to the mean-field (Fig. 3G) where the behavior stays close to the homogeneous solution in the bistable region (Fig. 3H), and then loses stability, but slightly lower  $J_0$  values than the mean-field.

We have shown that in the sLIF network, the loss of stability of the homogeneous solution occurs at a lower parameter value than where the limit cycle loses stability. Thus there is a parameter range where the stationary and oscillatory solutions coexist. We also demonstrate this bistability at set parameter values where a stimulus switches the network between the homogeneous and oscillatory states in both the mean-field approximation (Fig. 3I) and the sLIF network (Fig. 3J).

**3.4. Spatial instabilities.** Next, we investigate the instabilities induced by the spatial modulation of the coupling function. A spatial instability occurs when a non-zero spatial mode with zero temporal frequency becomes unstable. Recall that the amount of the spatial modulation of the synaptic coupling is given by the parameter  $J_1$ . Assuming k = 1 and  $\lambda_1 = 0$  in the dispersion relation (3.7) with cosine coupling (3.6) reveals the spatial instability at

$$(3.10) 4v_0 = J_1, \text{ if } J_1 > 4.$$



Bistability between high activity  $(v_+)$  and oscillatory states  $(v_{osc})$  with E=3 and D=2. A) The loss of stability of  $v_{osc}$  in the mean-field (2.2) (grey) at the fold of limit cycles and upper boundary of the bistable region (green) under slow ramp up of  $J_0$  (right arrow). The voltage is plotted against the current value of  $J_0$ , overlaid with the bifurcation diagram (black). B) A zoom in on the stable oscillation in the bistable region of the mean-field simulation (A, blue) C) Loss of stability of  $v_+$  (2.2) (grey) at the Hopf bifurcation and lower boundary of the bistable region (green) under slow ramp up of  $J_0$  (left arrow). D) A zoom in on the near homogeneous solution in the bistable region of the mean-field simulation (C, blue) in the same parameter range as (B). E) Same as (A) but with the sLIF network (2.1). F) A zoom in on the stable oscillation in the bistable region of the sLIF network simulation (E, blue) G) Same as (C) but with sLIF network. H) A zoom in on the near homogeneous solution in the bistable region of the sLIF network simulation (G, blue) in the same parameter range as (F). I) Homogeneous and oscillatory behavior of the mean-field equation at set parameters ( $J_0 = -3.04$ ). Pulses of amplitude 1 and -1 and duration 2 and 1.75 were applied to E at t = 25 and t = 62.5 to turn on (off) the oscillatory pattern. J) Homogeneous and oscillatory behavior in the spiking network at set parameters ( $J_0 = -3.22$ ). Pulses of amplitude 1 and -1 and duration 2 and 1 were applied to E at t = 25 and t = 58.

There is no spatial instability if  $J_1 \leq 4$ . It is an instability of  $v_+$  if  $J_0 < J_1/2$  and of  $v_-$  if  $J_0 > J_1/2$  (Fig. 4A, solid red and dashed red curves). The instability of  $v_+$  at the k=1 mode is a Turing bifurcation since the k=0 mode is still stable. Thus we call (3.10) with  $v_0 = v_+$  the Turing curve. The instability of  $v_-$ , on the other hand, is a secondary instability since the k=0 mode of  $v_-$  is already unstable.

The spatial instability switches from  $v_+$  to  $v_-$  at a codimension-2 bifurcation, where the Turing and saddle node curves meet tangentially (Fig. 4A, red and black curves). This occurs at the parameter values  $J_0 = J_1/2$  and  $E = J_0 - J_0^2/4$ . When  $J_0 = J_1/2$ , the k = 0 and k = 1 Fourier coefficients of the coupling function are equal and thus the saddle-node (instability of the k = 0 mode) and Turing (instability of the k = 1 mode) bifurcations coincide there.

The existence and location of the spatial instability curve depends on the amount of spatial modulation in the coupling function (Fig. 4B). A natural question is why  $J_1 = 4$  emerges as a critical value for the spatial instability defined by (3.10). This is

because at  $J_1=4$ , the spatial instability curve lies at the boundary of the regions of where  $v_{\pm}$  are above threshold (E=1). If  $J_1<4$ , then (3.10) is only defined in regions where  $v_{\pm}$  are below-threshold and no longer correspond to equilibria. We conclude that  $J_1$  must exceed this critical value  $(J_1>4)$  for pattern formation to occur. Additionally, the Turing bifurcation of  $v_{+}$  only occurs when the spatial coupling is either purely inhibitory  $(J_0<-|J_1|)$  or has local excitation and long range inhibition  $(|J_0|< J_1)$ . This is illustrated later in Figs. 6A and D (Section 3.5), which show the spatial instability curves in  $J_0, J_1$  plane.

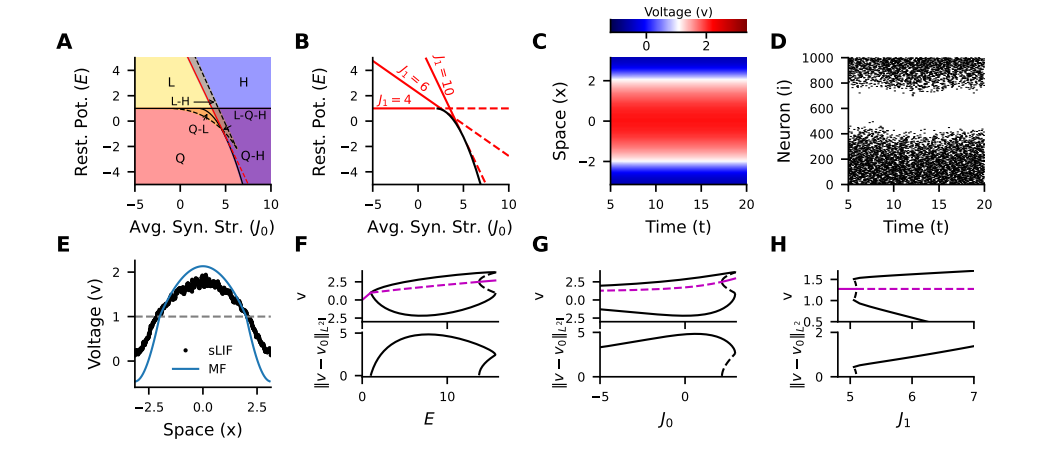


Fig. 4. A) Phase diagram in  $J_0$ , E plane showing quiescent (Q, red), high (H, blue), and local (L, yellow) activity regions. Bistable regions notated with a hyphen  $(e.g.\ Q-H)$ . B) Turing bifurcation of  $v_+$  (solid red), the spatial instability of  $v_-$  (dashed red), and saddle-node bifurcation (black), shown for  $J_1 = \{4,6,10\}$ . C) Stable bump solution from the mean-field model at E=3,  $J_0=-2$ ,  $J_1=8$ . D) Corresponding bump in a spiking network with N=1000. E) the comparison of the solution profiles of mean-field (blue) and sLIF network (black) from the simulations shown in (C) and (D) at t=20, smoothed over time and space, shown with the firing threshold (grey dashed). F-H) Bifurcation diagrams (top) showing the subcritical Turing bifurcation: bump amplitude (black lines, min/max) and homogeneous states (purple), with solid/dashed lines indicating stability. Bottom panels show the  $L^2$  norm  $||v-v_+||_{L^2(-\pi,\pi)}$  of the bumps solutions. Continuation shown with: F) varying E ( $J_0=5$ ,  $J_1=10$ ), G) varying  $J_0$  (E=5,  $J_1=10$ ), H) varying  $J_1$  (E=5,  $J_0=5$ ).

**3.4.1.** A bump solution. Beyond the instability of the first spatial mode, a stationary periodic bump solution exists (Fig. 4C). The bump profile has portions above and below threshold, corresponding to the active and inactive portions of the network. We therefore call this the local activity state (L). The sLIF network also exhibits local activity in a similar parameter regime (Fig. 4D), and the mean-field theory (4E, blue) gives a reasonable approximation to the activity of the spiking network (4E, black).

The Turing bifurcation is subcritical with a nearby fold of bump solutions. We used numerical continuation of the bump solution and determined the stability with numerical computation of eigenvalues for the mean-field linearization about the bump state (see Appendix 6.2). An unstable branch of small-amplitude bump solutions emerges backward when the active state  $v_+$  (Fig. 4F-H, purple) destabilizes through the Turing bifurcation as E or  $J_0$  decrease or  $J_1$  increases (Fig. 4F-H, dashed black). The numerical continuation revealed that any completely supra-threshold bump so-

lutions are unstable. When the minimum value of the unstable bump drops below threshold at v=1, it is shortly followed by the fold where it meets a stable branch of bump solutions. The stable branch extends off in both  $J_0$  (Fig. 4G) and  $J_1$  (Fig. 4H), but ends at a non-smooth Turing at E=1 when  $v_+$  drops below threshold (Fig. 4F).

**3.4.2.** Multi-stability with the bump. Due to the subcritical nature of the Turing bifurcation, there exists a bistable region of both the homogeneous and bump states between the bifurcation point and the fold. Within this region, networks can support either local or high activity behavior (Fig. 4A, "L-H"). Additionally, we find that in a small neighborhood of the codimension-2 bifurcation of the Turing and saddle-node, the non-smooth Turing is also subcritical with a nearby fold extending into the quiescent region (Fig. 5). This gives rise to two additional regions of multistability with the bump involving the quiescent state: a quiescent-local region and a local-quiescent-high region (Fig. 4A, "Q-L" and "L-Q-H") when the subcritical regions of the two bifurcations overlap. These regions are listed here for completeness. A detailed characterization of their boundaries is provided in the following section.

To summarize, we have identified four additional regions of the phase diagram (Fig. 4A) involving the bump solution:

- vii) L: A stable local (bump) solution exists.
- viii) L-H: Local (bump) and High  $(v_+)$  activity solutions exist and are stable.
- viii) Q-L: Stable Quiescent  $(v_Q)$  and Local (bump) solutions exist.
- ix) L-Q-H: Local (bump), Quiescent  $(v_Q)$ , and High  $(v_+)$  activity solutions exist and are stable.

The spiking network also exhibits multi-stability in these regions. First, we observe bistability between the local and high activity states, as predicted by the subcritical Turing bifurcation in the mean-field approximation described above (Fig. 5A). Additionally, we observe the bistability between the quiescent and local activity states (Fig. 5B), as predicted by the subcritical non-smooth Turing, and bistability between all three states (Fig. 5C).

3.4.3. Tracking the fold points to identify the boundaries of bistable regions. The regions Q-L and L-Q-H only exist in a small neighborhood near the co-dimension 2 bifurcation of the saddle-node and Turing bifurcations (Fig. 5D). The boundaries of these and the surrounding regions are defined by the various instabilities which occur in this neighborhood: the subcritical Turing bifurcation (Fig. 5D, solid red) and nearby fold of bump solutions (Fig. 5D, dashed green), the saddle-node bifurcation (Fig. 5D, solid black), and the subcritical non-smooth Turing (Fig. 5D, solid orange) with a nearby fold of the bump solutions (Fig. 5D, dashed blue). We refer to this second fold as the 'lower' fold since it occurs at lower E and  $I_0$  values than the 'upper' fold. Since both of the spatial instabilities are subcritical in this neighborhood, the boundaries of the stable bump region are determined by the folds.

To track the fold points and understand the interaction of various instabilities in this region, we computed bifurcation diagrams across a range of parameter values (Fig. 5E-L). These bifurcation diagrams are slices of the phase diagram (Fig. 5D) with an additional dimension showing v. The upper row (Fig. 5E-H), which shows continuation of the bump solution in the parameter E, are vertical slices of Fig. 5A at different  $J_0$  values. The lower row (Fig. 5I-L), showing continuation in  $J_0$ , are horizontal slices of Fig. 5A at various E values.

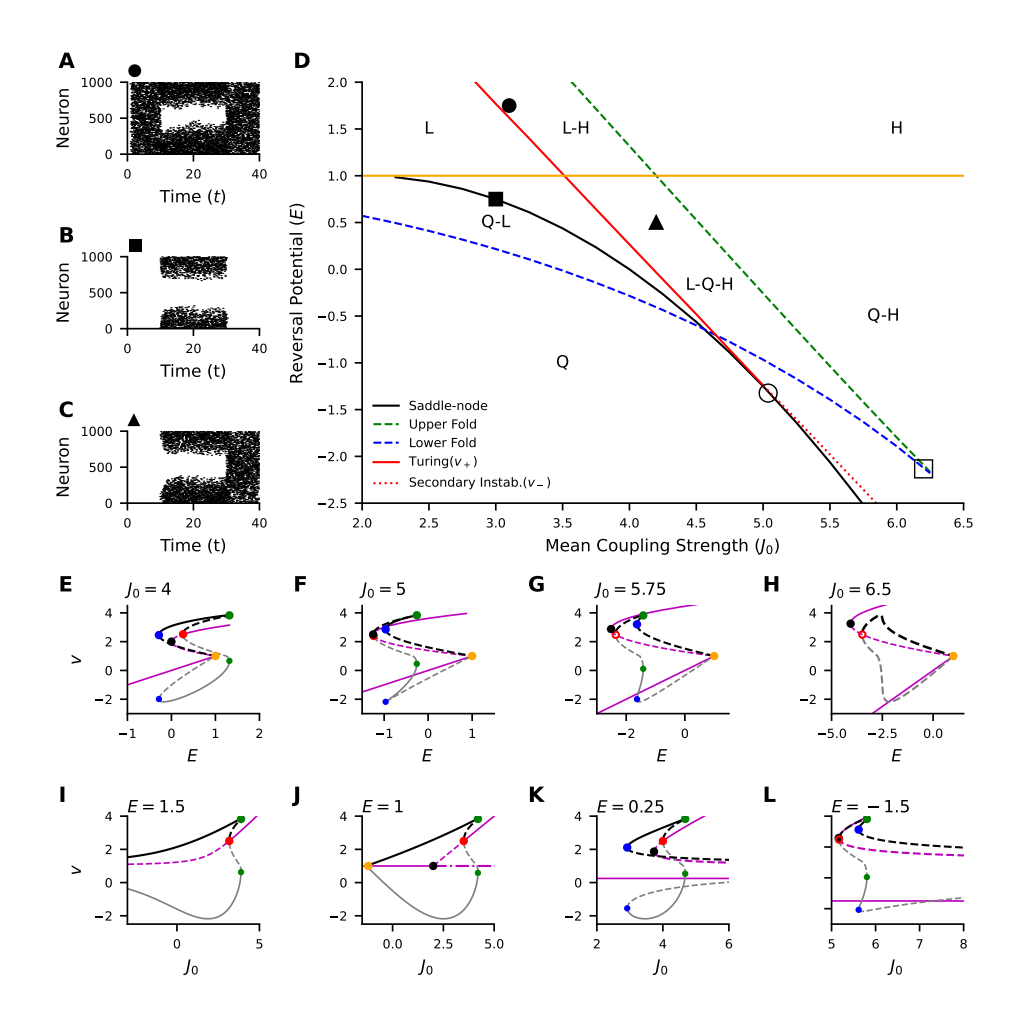


FIG. 5. Regions of multi-stability near codimension-2 bifurcations with  $J_1=10$ . **A-C**) Raster plots showing multi-stability of spiking network's activity at parameter locations marked in panel a. At t=15 and t=30, perturbations were applied to E. **D**) Phase diagram in  $J_0$ , E plane showing regions quiescent (Q), High (H), local (L) activity, and regions of bistability notated with a hyphens (e.g. Q-H) separated by various bifurcation curves. Turing bifurcation of  $v_+$  (red, solid), secondary spatial instability of  $v_-$  (red, dashed), fold of bump solution (green and blue, dashed), saddle-node bifurcation (black, solid), and 'non-smooth' saddle-node/Turing bifurcation (orange). The codimension 2 bifurcation of the simultaneous Turing and saddle-node bifurcations marked with an empty circle and the cusp-point of the two folds of bump solutions marked with an empty square. **E-H**) Bifurcation diagrams in parameter E at the  $J_0$  value written at top of panel. Colored circles corresponding to the various bifurcations curves shown in the phase diagram. **I-L**) Bifurcation diagrams in parameter  $J_0$  at the E value written at top of panel.

In each of these bifurcation diagrams, the instabilities' locations are marked with a circle whose color matches the corresponding curve in the phase diagram (Fig. 5D). For example, consider Fig. 5E, where five different instabilities (uniquely colored circles) are visible. The saddle-node bifurcation, where  $v_+$  and  $v_-$  collide and vanish, is marked with a black circle. The Turing bifurcation, where a unstable bump solution emerges from  $v_+$ , is shown with a red circle. Both a non-smooth Turing and saddle-

node bifurcation occur at the same point, shown with an orange circle, where  $v_-$ ,  $v_Q$ , as well as an unstable bump emerge as E is decreased. Lastly, there are two folds of the bump solution: the upper fold (green circle), connected to the Turing bifurcation via an unstable branch of bump solutions, and the lower fold (blue circle), connected to the non-smooth Turing via an unstable branch. The stable branch connecting the two folds determines where there is stable local activity.

All three regions of multi-stability with the bump solution are present when  $J_0=4$  (Fig. 5E). First, the L-H region, where only the bump solution and  $v_+$  are stable, lies between the non-smooth Turing bifurcation and the upper fold. The Q-L region, where there is bistability of  $v_Q$  and the bump solution, lies between the lower fold and the Turing bifurcation. The last region of multi-stability between three solutions (the bump,  $v_Q$ , and  $v_+$ ) lies between the Turing and non-smooth Turing bifurcations.

As  $J_0$  increases (Fig. 5F,  $J_0 = 5$ ), the L-H and Q-L regions vanish and L-Q-H is the only remaining multi-stable region with the bump. The two fold points (green and blue) have moved closer together and passed by the locations of the spatial instability (red) and the non-smooth Turing (orange). Therefore the stable branch of bump solutions between them is smaller and lies entirely in the region where both  $v_+$  and  $v_Q$  are also stable.

In addition to the loss of two of the bistable regions at  $J_0 = 4$ , the location of the spatial instability is now on the  $v_-$  branch after having just passed through the location of the saddle-node bifurcation (black circle) in a co-dimension 2 bifurcation. Despite being a secondary instability, the emerging branch of unstable bump solutions leads to a stable branch through a fold (Fig. 5F, green). We mark this secondary instability of  $v_-$  with an open red circle (largely obscured by the black circle) to distinguish it from the Turing bifurcation of  $v_+$  (marked with a solid red circle in the other panels).

If  $J_0$  is further increased (Fig. 5G,  $J_0 = 5.75$ ), the distance between the two folds continues to decrease and thus the size of the L-Q-H region decreases. They continue to approach each other until they collide and vanish in a codimension-2 cusp point (Fig. 5D, empty square) along with the stable branch between them, ending the L-Q-H region. Beyond the cusp point, an unstable branch of bump solutions remains, connecting the spatial instability to the non-smooth bifurcation (Fig. 5H,  $J_0 = 6.5$ ).

We can also see the emergence and disappearance of these bistable regions as the resting potential passes through threshold by looking at the continuation of the bump solution in the parameter  $J_0$ , at differing E values. When above threshold (E > 1, Fig. 5I), there is no lower fold and thus the only bistable region with local activity is L-H. The stable branch of bump solutions exists for all  $J_0$  values below the upper fold extending off to  $-\infty$  and slowly decreasing in amplitude as  $J_0$  is decreased. The stable branch also decreases in amplitude as E is decreased until at the threshold  $(E=1, \mathrm{Fig.} 5\mathrm{J})$ , it no longer extends to  $-\infty$  and instead meets  $v_Q$  at the non-smooth supercritical Turing bifurcation (Fig. 5J,  $J_0 \approx -1.3$ ). This is where the non-smooth Turing bifurcation becomes subcritical in the bifurcation parameter E and the lower fold emerges. Recall there are multiple transitions between homogeneous solutions at threshold. For  $J_0 < 2$ , the above threshold state  $v_+$  meets the below threshold state  $v_Q$  (i.e.  $v_+ = v_Q = 1$ ). For  $J_0 > 2$ , there is the non-smooth saddle bifurcation where both  $v_{-}$  and  $v_{Q}$  emerge. Thus the homogeneous solution at E=1 is stable for  $J_{0}<2$ and half-stable (dash-dotted) for  $J_0 > 2$ . Then below threshold (E < 1, Fig. 5K), there is a lower fold and an unstable branch of bump solutions that extends off to  $+\infty$ in  $J_0$ . Consequently, there are now Q-L and L-Q-H regions. As E decreases, the two folds move closer (Fig. 5L) leaving only the L-Q-H region. The folds eventually meet

in the codimension-2 cusp point (Fig. 5A, blue dashed, green dashed, empty square) ending the branch of stable bump solutions and local activity region.

**3.5.** Spatiotemporal instabilities. In the presence of both a delay and spatial modulation in the coupling, a spatiotemporal instability occurs and gives rise to spatiotemporal patterns. From the dispersion relation (3.7) we find the spatiotemporal instability in the first spatial mode (k = 1) at nonzero frequency  $(\text{Im}(\lambda_1) \neq 0)$ . It occurs when  $v_0$  is above threshold and

(3.11) 
$$\frac{-1}{D}\cos^{-1}\left(\frac{4v_0}{J_1}\right) = \frac{J_1}{2}\sqrt{1 - \left(\frac{4v_0}{J_1}\right)^2}.$$

This instability is a Turing-Hopf bifurcation of  $v_+$  if  $J_0 < J_*$  and a secondary instability of  $v_-$  if  $J_0 > J_*$ , where  $J_*$  is the  $J_0$  value of the codimension 2 point at which the Turing-Hopf curve and saddle-node curve intersect.

Four primary bifurcations occur throughout the phase space when  $D \neq 0$  and  $J_1 \neq 0$ : the saddle-node, Hopf, Turing, and Turing-Hopf bifurcations (Fig. 6A,B: blue, green, red, purple). The locations of these instabilities for any resting potential above threshold (E > 1), are topologically similar to Fig. 6A with different scaling dependent on E and the delay. Similarly, the locations of the instabilities when E < 1 are similar to Fig. 6B.

Formulaically, the Turing-Hopf curve (3.11) is similar to the Hopf curve (3.9). This is because they are both instabilities with non-zero frequencies, but at different spatial modes. Despite this, the Turing-Hopf curve increasingly resembles a reflection of the Turing curve across  $J_1 = 0$  as the delay increases. This becomes exact in the limit  $D \to \infty$ .

Beyond the Turing-Hopf bifurcation, we observe the emergence of standing and traveling waves (Fig. 6E, F) induced by the O(2) symmetry of J to translations and reflections in x. The sLIF exhibits both these patterns (Fig. 1G). In that simulation, a standing wave spontaneously transitions into a traveling wave, suggesting metastability in the sLIF network. Bistability of the standing and traveling waves with other states of the network remains to be investigated, and could be done using numerical continuation of solutions implementing both delays and spatial modulation. This is the final region of the phase diagram we describe:

# x) SW-TW: Standing and traveling waves exist and are stable.

In regions beyond multiple primary instabilities, both the mean-field approximation and sLIF network exhibit a variety of additional spatiotemporal patterns, some likely arising from secondary or higher-order bifurcations. Beyond both the Turing and Hopf bifurcations, we observe an oscillatory bump (Fig. 6H, I). Beyond the Turing-Hopf bifurcation, we observe additional types of dynamics likely due to an additional instability (Fig. 6P-Q). Finally, beyond both the Turing-Hopf and Hopf bifurcations, we observe a variety of mixed mode oscillations (Fig. 6J-S). Investigating these secondary instabilities and the rich variety of dynamical patterns to which they lead remains a direction for future research.

4. More realistic synaptic responses. Synaptic potentials are characterized by three time scales: the latency or transmission delay (the time between the presynaptic spike emission and the postsynaptic response), as well as the rise time and the decay time [18]. So far for the temporal profile, we have studied delayed pulse

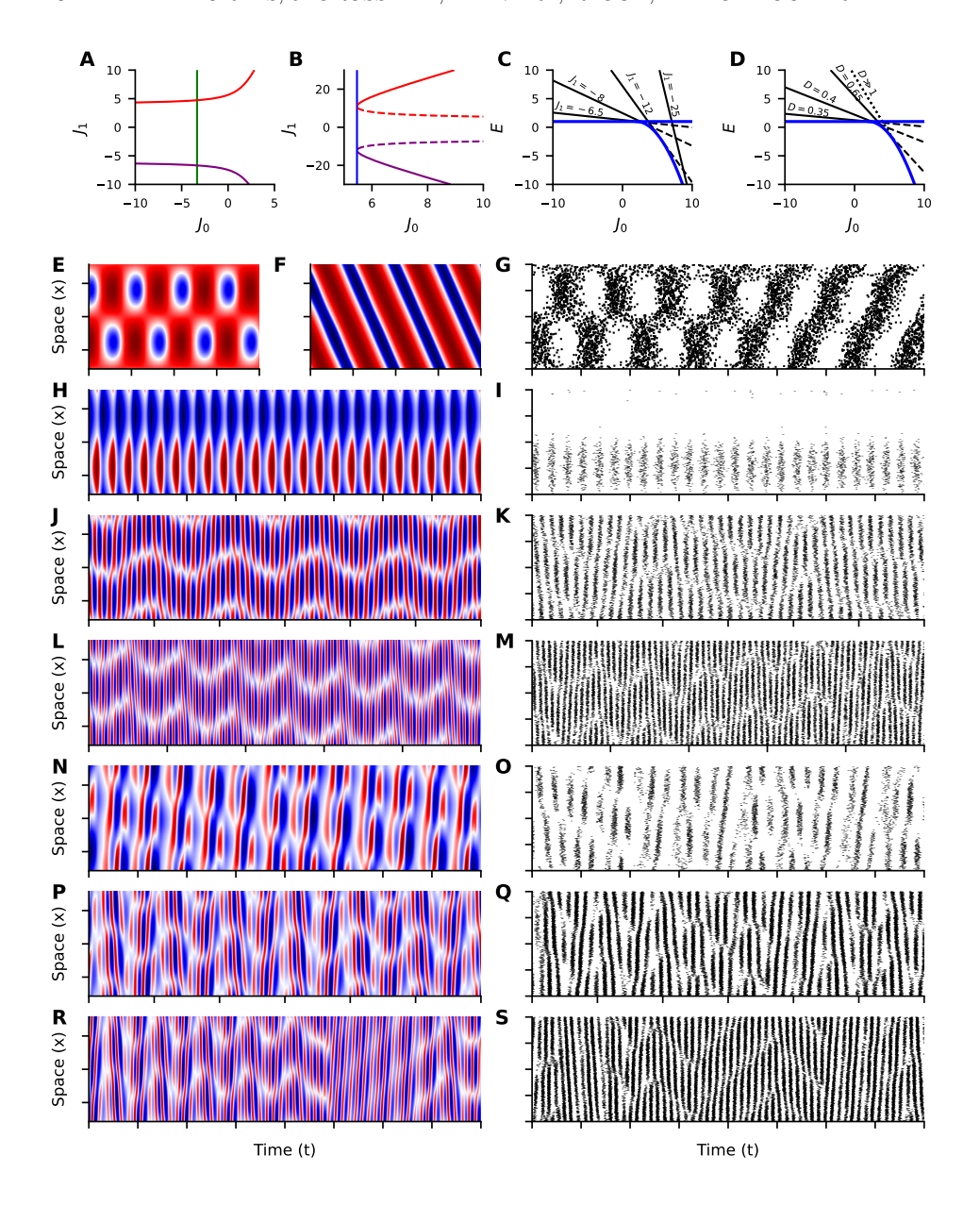


FIG. 6. Spatiotemporal instabilities and patterns in the mean-field approximation (2.2) and the sLIF network (2.1). A) Primary instabilities at E=2, D=1: Turing (red), Hopf (green), and Turing-Hopf (purple). B) Same as A, but at E=-2: includes Saddle (blue), and Turing-Hopf of  $v_+$  (solid) and  $v_-$  (dashed). C-D) Turing-Hopf curves in the  $J_0$ , E plane, varying  $J_1$  (C) and delay D (D). E-F) Standing (E) and traveling (F) waves at  $J_0=-2$ ,  $J_1=-8$ , E=2, D=1. G) sLIF simulation under same parameters as E-F. H-I) Oscillatory bump beyond Turing and Hopf:  $J_0=-60$ ,  $J_1=20$ , E=10, D=0.2. J-S) Additional spatiotemporal patterns at E=10, D=0.2: J-K)  $J_0=-17$ ,  $J_1=-60$ ; L-M)  $J_0=-16$ ,  $J_1=-72$ ; N-O)  $J_0=-25$ ,  $J_1=-95$ ; P-Q)  $J_0=-5$ ,  $J_1=-100$ ; R-S)  $J_0=-15$ ,  $J_1=-100$ .

coupling, which models just the transmission delay. We next consider two additional forms for the temporal coupling which also model the rise and decay times of the synaptic potential. The first is the delayed exponential

(4.1) 
$$J_{\text{time}}(t-D) = \frac{J_0}{\tau} e^{-(t-D)/\tau} H(t)$$

where H is the Heaviside step function. This kernel implements a decay time of the action potential in addition to the delay (Fig. 7A). The additional decay time smooths the postsynaptic response to incoming spikes compared to pulse coupling (Fig. 7B). The locations of the four primary instabilities are very similar to the pulsed coupling case (Fig. 7C and D).

The delayed alpha function (Fig. 7E) is another option for the temporal profile which also includes the rise time of the synaptic potential. It is defined by

(4.2) 
$$J_{\text{time}}(t-D) = \frac{J_0}{\tau^2}(t-D)e^{-(t-D)/\tau}H(t-D).$$

This synaptic kernel further smooths the change in voltage of the postsynaptic neuron upon the arrival of a spike (Fig. 7F). Again, the instability diagrams are qualitatively similar to the two previous cases of temporal kernels (Fig. 7G and H). Notably, a nonzero delay is not required for the existence of a Hopf bifurcation and homogeneous oscillatory behavior with this temporal profile. The rise time of the alpha function acts as an effective delay in the transmission of action potentials between neurons.

Due to the similarity of instability diagrams for these other synaptic response functions, we expect similar dynamics arising at onset. See Appendices 6.5 and 6.6 for the derivation of the dispersion relations and instability curves for these cases.

5. Discussion. Patterns in neural activity are classically modeled using neural field equations such as the Wilson-Cowan and Amari-Grossburg models [54, 2, 28]. These can be derived as explicit mean-field theories for highly simplified microscopic models or by making strong assumptions like a separation of timescales between neural and synaptic dynamics [39, 26, 9, 41]. This complicates their relation to biophysical microscopic models. This discrepancy is one motivation for the development of next-generation neural field theories from specific microscopic models [36, 46, 10].

Soft-threshold integrate-and-fire networks replace the nonlinear dynamics of spike emission with a probabilistic spike-and-reset rule, but other biophysical detail can be directly incorporated. This family of models is often studied with a population density approach, which exposes rigorous mean-field limits [25, 17]. The mean-field limit can also be exposed through the joint density functional of network, rather than the population density [42, 38]. The population density approach has recently been extended to networks with either spatial connectivity or delays, exposing Hopf or Turing bifurcations separately [33, 20, 19, 16].

Here, we instead used a deterministic approximation to study the dynamics of soft-threshold leaky integrate-and-fire (sLIF) networks with both synaptic delays and spatial connectivity. This approximation has a similar form to the classic Amari-Grossberg equations with an additional term due to the voltage resets after action potentials. We found oscillatory, spatial, and spatiotemporal instabilities that generate coherent activity patterns such as bulk oscillations, standing bumps, standing and traveling waves. We identified various multi-stable regions of different network states due to the sub-criticality of the Hopf and Turing bifurcations. In these regions, the network can support both patterned behavior and a homogeneous state (quiescent or

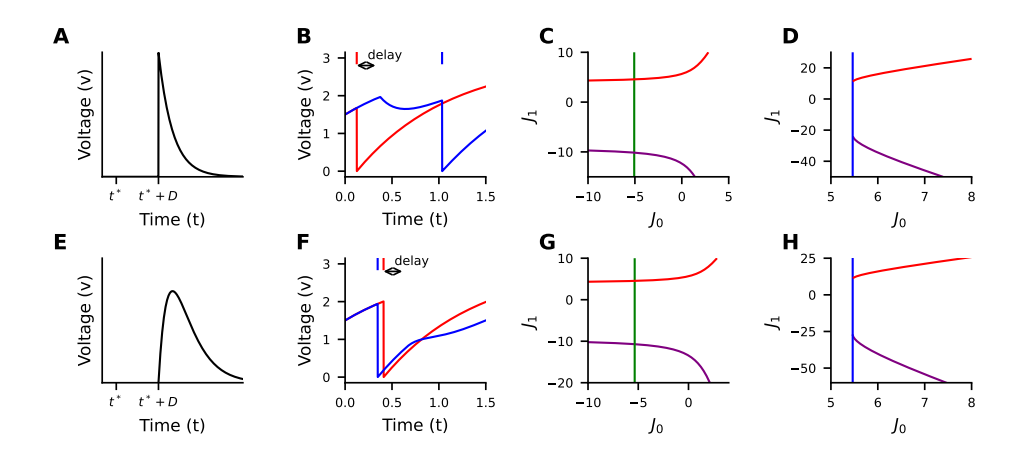


FIG. 7. Instabilities with other temporal coupling profiles. A) The delayed exponential profile (4.1) B) presynaptic neuron (red) emits a spike causing a change in membrane voltage of postsynaptic neuron (blue) after the delay. C) Primary instabilities present above threshold with the delayed exponential: Hopf(green), Turing(red), Turing-Hopf(purple), E=2, D=1, and  $\tau=1$ . D) Primary instabilities present below threshold with the delayed exponential: Saddle(blue), Turing(red), Turing-Hopf(purple), E=-2, D=1, and  $\tau=1$ . E) The delayed alpha function (4.2). F) Presynaptic neuron (red) emits a spike causing a change in membrane voltage of postsynaptic neuron (blue) after the delay. G) Primary instabilities present above threshold with the alpha function: Hopf(green), Turing(red), Turing-Hopf(purple), E=2, D=1, and  $\tau=1$ . H) Primary instabilities present below threshold with the alpha function: Saddle(blue), Turing(red), Turing-Hopf(purple), E=-2, D=1, and  $\tau=1$ .

active), and can be switched from one state to the other by global or local perturbations. We confirmed all these predictions of the mean-field dynamics in simulations of the underlying microscopic stochastic system.

The classic neural field equation,  $\partial_t x = -x + f(E + J * x)$  on the ring, has similar transitions from a homogenous equilibrium to oscillatory and bump solutions in the presence of delays and spatially modulated coupling [44, 4]. The locations of those bifurcations differ in the classic rate and sLIF networks, however. For example, in the classic neural field equation the Turing instability of the homogenous active state occurs at  $J_1 = 2$ ; in the sLIF mean-field dynamics we studied, the Turing instability occurs at  $2J_1 = J_0 + \sqrt{J_0^2 + 4(E - J_0)}$  ((3.10)). Secondary bifurcations and codimension-2 points also differ between the two models.

From a mathematical point of view, all of the primary bifurcations we described could be studied using a parameter dependent infinite-dimensional center manifold reduction [30, 52, 3]. When J has no delay, the bifurcating eigenvalues in each case are discrete, with finite multiplicity and a spectral gap to the rest of the spectrum, all of which lies in the left half plane. One would derive a finite-dimensional ODE system which unfolds the various bifurcations, as well as their codimension-two points, and rigorously establishes the non-trivial states (oscillations, periodic pattern, etc.). Due to the lack of other positive spectrum of the homogeneous equilibrium at the bifurcation, one can use invariant foliations to show the center manifold attracts all nearby trajectories, and hence that stability on the manifold implies local stability in the full PDE. It would then be of interest to see if higher order expansions and/or analytic continuation could be used to capture the large amplitude fold state.

The sLIF networks we studied are members of a broader family of soft-threshold integrate-and-fire networks with richer voltage dynamics. Soft-threshold integrate-and-fire networks with nonlinear voltage dynamics can have oscillatory solutions [16]. Adaptive exponential integrate-and-fire neurons can capture a broad range of single-neuron spike patterns [37, 49]. Adaptive nonlinear soft-threshold integrate-and-fire networks are also amenable to the same type of mean-field approximation we used here. Including excitatory and inhibitory cell types and their relative spatial coupling profiles and synaptic timescales may also give rise to new spatiotemporal dynamics [31].

Furthermore, it would be of interest to consider these patterns on unbounded domains as well as infinite dimensions. Near the Turing instabilities found here, we expect a family of (subcritical) periodic waves to bifurcate. The subcriticality and bistability in the bounded domain problem indicates it should be possible in the unbounded domain to construct fronts connecting the periodic state to the quiescent state, localized patterns, and other complex modulated waves [23, 24].

Next-generation neural field theories also aim to explicitly describe fluctuations, correlations, and synchrony [10]. The neural field equations we study can be straightforwardly extended to include these through a fluctuation expansion of the density functional of the underlying microscopic model [38, 9, 6]. For the sLIF networks studied here, there are three possible types of fluctuation correction: 1) corrections to the mean-field rate  $f(\bar{v})$  due to fluctuations in the voltage, 2) a correction to the mean-field voltage dynamics due to the spike-voltage covariance, and 3) variability in the synaptic field due to correlated or finite-size fluctuations in the activity. These have each been studied in non-spatial networks [38, 40, 45]. How these different fluctuations interact with neural nonlinearities to shape spatiotemporal patterns in sLIF networks remains to be investigated.

## Declarations.

Authorship:. All authors have made substantial intellectual contributions to the study conception, execution, and design of the work. All authors have read and approved the final manuscript. In addition, the following contributions occurred: Conceptualization: Ryan Goh, Gabriel Koch Ocker; Formal analysis and investigation: Lauren Forbes, Jared Grossman, Ryan Goh; Writing - original draft preparation: Lauren Forbes; Writing - review and editing: Lauren Forbes, Ryan Goh, Gabriel Koch Ocker; Supervision: Montie Avery, Ryan Goh, Gabriel Koch Ocker.

Conflicts of interest:. The authors declare no conflicts of interest.

 $\label{eq:def:Data} \textit{Data and code availability:.} \end{code to reproduce the results of this manuscript can be found at $https://github.com/lcforbes4/sLIFspatioTemporal}$ 

Funding:. The research of the authors was partially supported by NSF-DMS 2307650 (RG), and by a grant from the Allen Institute Mindscope Phase 4 program (GKO).

#### 6. Appendix.

**6.1. Further reading.** We used largely standard methods for linear stability analysis of partial differential equations and numerical continuation, as described in [14, 5, 50]. In the following sections, we describe these computations in detail.

### 6.2. Numerical methods.

**6.2.1. Simulations.** Simulations of the mean-field approximation (2.2) were done using the forward Euler method with a step size of dt = 0.001. The ring  $(0, 2\pi]$  was descritized as  $x_i = -\pi + \frac{2\pi}{N}i$ , i = 1, ..., N, and N = 100 (N = 1000 for MF simulations of spatiotemporal dynamics in Fig. 6).

Simulations of the sLIF network (2.1) were done using the stochastic forward Euler method with step size dt = 0.001 with N = 1000. The spatial coupling was implemented within the randomly sparse connectivity matrix  $\mathbf{J} \in \mathbb{R}^{N \times N}$ . The connections between neuron pairs (i,j) were independently sampled as Bernoulli random variables with probability p = 0.5. Each connection has synaptic weight given by  $J_{ij} = \frac{2\pi}{pN}(J_0 + J_1\cos(x_i - x_j))$ . Self-connections are excluded by setting  $J_{ii} = 0$ . We generated spikes by sampling  $dn_i$  as Bernoulli random variables at each time step with success probabilities  $f(v_i)dt$ . Finally, synaptic delays were incorporated with a time-shift of  $N_{\text{delay}} = |D/dt|$  to the synaptic input.

The initial conditions must be defined for  $t \in [-D, 0]$  due to the presence of the delay. Most patterns were initialized with constant initial conditions or the stationary form  $A + B\cos(x)$ . For the traveling wave pattern seen in Fig. 6F, we used an initial condition of the form  $A + B\cos(x + tv)$  with  $v \neq 0$  to induce wave propagation. Details for specific initial conditions are found in the code repository https://github.com/lcforbes4/sLIFspatioTemporal.

**6.2.2.** Inducing network transitions in bistable regions. To switch from the high activity state to the oscillatory state (Fig. 3 I-J), a positive pulse with short duration was applied to the entire network. To turn off the oscillatory state and return to the high activity state, a negative pulse was applied during the peak of the oscillations to suppress oscillatory activity. The timing, amplitude, and duration of the negative pulse were fine tuned to the particular simulation and set of parameters to achieve the return to the high activity state. See figure caption for specific pulse parameters.

In all three simulations (Fig. 5A–C), a spatially dependent drive of the form  $-2\cos(x)$ , applied for a duration of 1, was used to induce a transition to local network activity. To transition from the local activity state to the high activity state (Fig. 5, A and C), a pulse with amplitude -2 was applied to the quiescent middle third of the network (neurons [N/3:2N/3]). To transition from the local activity state to the quiescent state (Fig 5 B), a pulse with amplitude -2 was applied to the active outer two thirds of the network (neurons [0:N/3] and [2N/3:N]).

**6.2.3.** Continuation of oscillatory solutions. Continuation of oscillatory solutions was performed using a one-dimensional, spatially homogeneous mean-field reduction (2.2). This approximation assumes zero spatial modulation ( $J_1 = 0$ ) in the coupling function, such that each neuron in the network evolves according to the spatially independent delay-ODE. We used the MATLAB package DDE-Biftool, which was developed for bifurcation analysis of delay differential equations (DDEs)([21] [47]). First, we computed and continued a branch of equilibria along with the spectrum of its linearization to identify the location of the Hopf bifurcation. Then we initialized

a small-amplitude orbit near the Hopf bifurcation to construct and continue a branch of oscillatory solutions. Stability of periodic orbits was determined by simultaneously computing Floquet multipliers of the linearized periodic map.

**6.2.4. Continuation of bump solutions.** The periodic bump solutions computed in Section 3.4 are steady-state solutions of the mean-field approximation (2.2) with spatial connectivity  $(J_1 \neq 0)$  but without delay (D = 0). To compute these solutions numerically in MATLAB, we discretized (2.2) using a Fourier spectral method with  $N = 2^{12}$  modes on the periodic domain  $[0, 2\pi)$ . We denote the discretized time-independent version of (2.2), as the non-linear system  $F_1(v) = 0$  where  $v \in \mathbb{R}^N$  is the spatially discretized steady-state solution.

To obtain a good initial guess for the bump, we ran a short Euler time-stepper initialized with a small perturbation (of order  $10^{-1}$ ) of the spatially homogeneous steady state. To fix the continuous translational symmetry on the ring, we appended the following phase condition on our system

$$F_2(v) = \langle u(x), \sin(x) \rangle_{L^2} = 0,$$

which pins the solution, and modified  $F_1$  with an additional drift term  $c\partial_x v$ . The imposition of this condition requires an additional unknown or dummy variable c. We then solved the resulting augmented system  $F(v,c) = \begin{bmatrix} F_1(v) + c\partial_x v \\ F_2(v) \end{bmatrix} = 0$  for v and v using a Newton–GMRES method, where vector products in the Jacobian were computed spectrally and GMRES without preconditioning was used to compute the Newton step.

Once the initial bump solution was obtained, we performed numerical continuation in a single bifurcation parameter  $\beta$  using secant continuation. To do this, we introduced the augmented variable  $z=[v,c,\beta]$  and appended the orthogonality condition

$$F_3(z) = \langle z - z_0, sec \rangle = 0,$$

where  $z_0 = [v_0, c_0, \beta_0]$  is the previously computed solution in the continuation and  $sec \in \mathbb{R}^{N+2}$  is the normalized secant vector between the two most recent solutions. The variable c stays uniformly close to zero throughout the continuation. The complete augmented system used for secant continuation is then

$$F(z) = \begin{bmatrix} F_1(v) + c\partial_x v \\ F_2(v) \\ F_3(z) \end{bmatrix} = 0 \text{ where } z = [v, c, \beta].$$

At each step of the continuation, we computed the spectral stability of the linearized operator near the origin with leading eigenvalues of Jacobian of the original system  $F_1$  (without the phase and orthogonality conditions) and Matlab's eigs function. In Fig. 8, we plot the real part of the eigenvalues with  $Re(\lambda) > -5$  along the entire continuation curve in the parameter E. The continuation starts at the Turing bifurcation and initially has an eigenvalue with  $Re(\lambda) > 0$ , indicating instability and likely a subcritical bifurcation. When the largest eigenvalue drops below zero (which occurs near E = 2.90), marks the location of a fold of bump solutions and the continuation's switch onto the stable branch at the upper fold. The continuation then follows the stable branch until the lower fold where a real part of an eigenvalue becomes positive (E = 0.22) and solutions are unstable until terminating at the non-smooth Turing bifurcation. The eigenvalue with  $Re(\lambda) = 0$ , which remains present throughout the

continuation, is a consequence of the translational invariance of solutions on the ring. The locations of the two fold curves in the phase diagram in Fig. 5D were identified by determining the location of the fold in multiple single-parameter continuations of the bump solution at varying parameters, not through continuation of the fold itself.

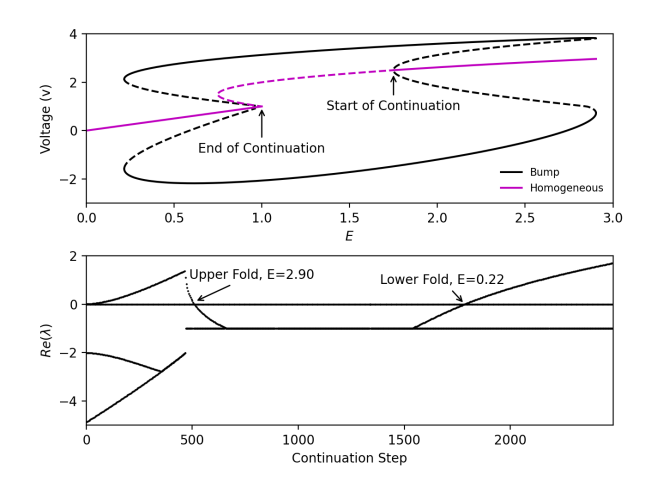


Fig. 8. Tracking eigenvalues along the continuation of the bump solution.

**6.3. General dispersion relation.** To derive the dispersion relationship, we consider the mean-field approximation with a general coupling function J(x, t - D) where  $J(x,t) \in L^1((-\pi,\pi) \times (0,\infty))$  along with the intensity function f(v(x,t)), (6.1)

$$\partial_t v(x,t) = -v(x,t) + E - f(x,t) v(x,t) + \int_{-\infty}^{t-D} \int_{-\pi}^{\pi} J(x-y,t-s-D) f(y,s) dy ds$$

with periodic spatial domain,  $x \in (-\pi, \pi]$ . Assuming  $v = v_0 + \epsilon w$ , we linearize (6.1) about its stationary uniform solution,  $v_0 = E - v_0 f(v_0) + (J * f(v_0))(x, t - D)$ , (6.2)

$$\partial_t w = (-1 - f(v_0) - v_0 f'(v_0)) w + f'(v_0) \int_{-\infty}^{t-D} \int_{-\pi}^{\pi} J(x - y, t - s - D) w(y, s) \, dy \, ds$$

Taking the Fourier transform of (6.2) in space results in the following system of differential equations indexed by the wave number k

(6.3) 
$$\partial_t \hat{w}_k = (-1 - f(v_0) - v_0 f'(v_0)) \hat{w}_k + f'(v_0) \int_{-\infty}^{t-D} \hat{J}_k(t - s - D) \hat{w}_k(s) ds$$
,  $k \in \mathbb{Z}$ 

where  $\hat{w}_k(t) = \int e^{-ikx} w(x,t) dx$  and  $\hat{J}_k(t) = \int e^{-ikx} J(x,t) dx$  are the time-dependent  $k^{th}$  Fourier coefficients of w and J. Finally, making the ansatz  $\hat{w}_k = e^{\lambda_k t}$  and the substitution  $\tilde{s} = t - s - D$ , we get the dispersion relation

(6.4) 
$$\lambda_k = -1 - f(v_0) - v_0 f'(v_0) + f'(v_0) e^{-\lambda_k D} \int_0^\infty \hat{J}_k(\tilde{s}) e^{-\lambda_k \tilde{s}} d\tilde{s}$$

Note that with the additional assumption of a threshold linear intensity function of the form  $f(v) = \lfloor v - 1 \rfloor_+$ , (6.4) simplifies to (3.3).

**6.4. Instabilities with delayed pulse coupling.** To derive the dispersion relation for delayed pulse coupling, we assume  $\hat{J}_k(t) = \hat{J}_k\delta(t)$ ,  $f(v) = [v-1]_+$ , and  $v_0 > 1$ . The dispersion relation (6.4) then simplifies to

$$\lambda_k = -2v_0 + \hat{J}_k e^{-\lambda_k D}$$

Separating the real and imaginary components of (6.5) and assuming the instability condition  $Re(\lambda_k) = 0$ ,

(6.6a) 
$$\begin{cases} 0 = -2v_0 + \hat{J}_k \cos(-D\lambda_{i,k}) \\ \lambda_{i,k} = \hat{J}_k \sin(-D\lambda_{i,k}) \end{cases}$$

where  $\lambda_{i,k} := Im(\lambda_k)$ . We remark that the eigenvalue equation can also be formulated with the Lambert W equation [15] to achieve the same results. From now on, we assume the Fourier coefficients of cosine spatial coupling (3.6) which are  $\hat{J}_0 = J_0$ ,  $\hat{J}_{\pm 1} = J_1/2$ , and  $\hat{J}_k = 0 \,\forall k \notin \{0, \pm 1\}$ . We next identify the locations of four instabilities of the stationary uniform equilibria  $v_{\pm}$  given in (3.1).

I. Saddle-node Bifurcation ( $k = 0, \lambda_{i,0} = 0$ ): This is an instability of the k = 0 mode with zero temporal frequency. Given that the imaginary part of the eigenvalue is zero, (6.6b) is trivial. Then by substituting the form of  $v_{\pm}$  given in (3.1), (6.6a) simplifies to  $J_0 = 2 \pm 2\sqrt{1-E}$ . Note that in the minus case, neither  $v_{\pm}$  are above threshold and thus are not equilibria. Therefore the instability only occurs along the curve

$$(6.7) J_0 = 2 + 2\sqrt{1 - E}$$

II. Hopf Bifurcation  $(k = 0, \lambda_{i,0} \neq 0)$ : This is an instability of the k = 0 mode with non-zero temporal frequency. We solve (6.6a) for  $\lambda_i$  yielding  $\lambda_i = \frac{-1}{D} \cos^{-1}(\frac{2v_0}{J_0})$ , using the principle branch of  $\cos^{-1}$ . Substituting this form of  $\lambda_i$  into (6.6b) gives the Hopf curve as an implicit function of the parameters

(6.8) 
$$\frac{-1}{D}\cos^{-1}\left(\frac{2v_0}{J_0}\right) = J_0\sqrt{1 - \left(\frac{2v_0}{J_0}\right)^2}$$

We show below that only  $v_+$  can undergo a Hopf Bifurcation if  $3J_0^2 + 4J_0 > 4E$ ,  $v_+ > 1$ , and  $J_0 < 0$ . Using the expression for  $v_{\pm}$  in terms of the parameters given in (3.1), the real part of the dispersion relation (6.6a) simplifies to

(6.9) 
$$1 \pm \frac{|J_0|}{J_0} \sqrt{1 + \frac{4(E - J_0)}{J_0^2}} = \cos(-D\lambda_i)$$

Due to the range of cosine, (6.9) is only well defined for the minus case (instability of  $v_{-}$ ) if  $J_0 > 0$ . (6.9) is well defined for the plus case (instability of  $v_{+}$ ) if  $J_0 < 0$ . But since the principle branch of arccosine is a non-negative function, the Hopf curve given in (6.8) is only well defined for  $J_0 < 0$ . Therefore, we conclude that only  $v_{+}$  can undergo a Hopf bifurcation.

Finally, to satisfy the domain of arccosine, we have the condition

(6.10) 
$$\left| \frac{2v_0}{J_0} \right| = \left| \frac{J_0 + \sqrt{J_0^2 + 4(E - J_0)}}{J_0} \right| < 1$$

which can be rewritten as the set of inequalities  $3J_0^2 + 4J_0 > 4E$ ,  $v_+ > 1$ , and  $J_0 < 0$ . We note that using implicit differentiation, one can also show the transverse crossing condition of a Hopf bifurcation is satisfied along the curve (6.8). Additionally, for  $D \gg 1$ , the Hopf Curve lies approximately at  $3J_0^2 + 4J_0 = 4E$ .

III. Turing Bifurcation  $(k=1, \lambda_{i,1}=0)$ : This is an instability of a non-zero mode with zero temporal frequency. Similar to the saddle-node bifurcation case, since the imaginary part of the eigenvalue is zero, (6.6b) is trivial and (6.6a) simplifies to  $2v_0 = J_1/2$ . Note that  $v_0 > 1$  only if  $J_1 > 4$ . Therefore, there is a spatial instability of  $v_{\pm}$  at

(6.11) 
$$\pm \sqrt{J_0^2 + 4(E - J_0)} = J_1/2 - J_0 \text{ if } J_1 > 4$$

This can be rewritten as

(6.12) 
$$E = J_1^2/4 + J_0(4 - J_1)$$

which corresponds to the Turing Bifurcation of  $v_{+}$  if  $J_{0} < J_{1}/2$  and a secondary instability of  $v_{-}$  if  $J_0 > J_1/2$ .

IV. Turing-Hopf  $(k=1,\lambda_{i,1}\neq 0)$ : This is an instability of a non-zero mode with non-zero temporal frequency. Similar to the Hopf bifurcation case, we substitute  $\lambda_{i,1} = \frac{-1}{D}\cos^{-1}(\frac{2v_0}{J_0})$  from (6.6a) into (6.6b). This gives the curve of a spatiotemporal instability of  $v_0$ 

(6.13) 
$$\frac{-1}{D}\cos^{-1}\left(\frac{4v_0}{J_1}\right) = \frac{J_1}{2}\sqrt{1-\left(\frac{4v_0}{J_1}\right)^2}$$

if  $v_0 > 1$  as well, which occurs if  $\frac{J_1}{4}\cos(D\lambda_{i,1}) > 1$  from (6.6a). Note that this curve intersects the saddle-node curve in a codimension-2 bifurcation if  $J_0 = \frac{J_1}{2}\cos(-D\lambda_{i,1})$ . The instability (6.13) is a Turing-Hopf bifurcation of  $v_+$ if  $J_0 < \frac{J_1}{2}\cos(-D\lambda_{i,1})$  and a secondary instability of  $v_-$  if  $J_0 > \frac{J_1}{2}\cos(-D\lambda_{i,1})$ .

6.5. Instabilities with delayed exponential coupling. To identify the locations of instabilities with the delayed exponential temporal profile of the coupling, ie  $\hat{J}_k(t) = \hat{J}_k \tau^{-1} e^{-(t)/\tau} H(t)$ , we assume  $f(v) = [v-1]_+$  and  $v_0 > 1$ . The dispersion relation (6.4) then simplifies to

(6.14) 
$$\lambda_k = -2v_0 + \hat{J}_k e^{-\lambda_k D} \frac{1}{(1 + \lambda_k \tau)}$$

Separating the real and imaginary components of (6.14) with the assumption  $Re(\lambda_k) =$ 0 results in

(6.15a) 
$$\begin{cases} -\tau \lambda_{i,k}^2 = -2v_0 + \hat{J}_k \cos(\lambda_{i,k}D) \\ \lambda_{i,k} = \hat{J}_k \sin(-\lambda_{i,k}D) - 2v_0 \lambda_{i,k}\tau \end{cases}$$

(6.15b) 
$$\lambda_{i,k} = \hat{J}_k \sin(-\lambda_{i,k}D) - 2v_0 \lambda_{i,k} \tau$$

Note that when  $\lambda_{i,k} = 0$ , (6.14) is equivalent to (6.5). Therefore the instabilities with zero temporal frequency occur along the same curves as the delayed pulse case. The saddle-node bifurcation in the delayed exponential case is then also given by (6.7) and the Turing bifurcation is given by (6.12).

To identify the locations of instabilities with non-zero temporal frequencies, first rewrite (6.15b) as  $\lambda_i = \hat{J}_k \sin(-\lambda_{i,k}D)/(1+2v_0\tau)$  and substitute it into (6.15a) to get

$$-\tau \left(\frac{\hat{J}_k \sin(-\lambda_{i,k} D)}{1 + 2v_0 \tau}\right)^2 = -2v_0 + \hat{J}_k \cos(\lambda_{i,k} D)$$

Then, by using the identity  $\sin^2(x) = 1 - \cos^2(x)$  and defining  $y := \cos(\lambda_{i,k}D)$ , we can transform the equation above into the quadratic

$$(-\hat{J}_k^2\tau)y^2 + (\hat{J}_k + 4v_0\tau\hat{J}_k + 4v_0^2\tau^2\hat{J}_k)y + (\tau\hat{J}_k^2 - 2v_0 - 8v_0^2\tau - 8v_0^3\tau^2) = 0$$

We solve this quadratic for y and thus for  $\lambda_{i,k} = D^{-1} \arccos(y)$ 

(6.16) 
$$\lambda_{i,k} = \frac{1}{D} \arccos\left(\frac{(1+4v_0\tau + 4v_0^2\tau^2)}{2\hat{J}_k\tau}\right) \\
\pm \frac{\sqrt{(1+4v_0\tau + 4v_0^2\tau^2)^2 + 4\tau(\tau\hat{J}_k^2 - 2v_0 - 8v_0^2\tau - 8v_0^3\tau^2)}}{2\hat{J}_k\tau}\right)$$

Plugging this  $\lambda_i$ , which is in terms of the parameters  $\hat{J}_k, E, \tau, D$ , into the imaginary part of our dispersion relation (6.15b) gives

(6.17) 
$$\operatorname{arccos} \left( \frac{A\hat{J}_k \pm |\hat{J}_k| \sqrt{A^2 + 4\tau(\tau \hat{J}_k^2 - 2v_0 A)}}{2\hat{J}_k^2 \tau} \right) (1 + 2v_0 \tau)$$

$$= -\hat{J}_k D \sqrt{1 - \left( \frac{A\hat{J}_k \pm |\hat{J}_k| \sqrt{A^2 + 4\tau(\tau \hat{J}_k^2 - 2v_0 A)}}{2\hat{J}_k^2 \tau} \right)^2}$$

where  $A=1+4v_0\tau+4v_0^2\tau^2$ . This is the Hopf curve when k=0 and  $\hat{J}_k=J_0$  or the Turing-Hopf curve when k=1 and  $\hat{J}_k=J_1/2$ .

Next, we will look at which parameter values and which equilibria  $v_0$  the curve (6.17) is well defined for. First, we note that the range of the principle branch of arccosine is non-negative, so (6.17) is not defined for  $\hat{J}_k > 0$ .

To satisfy the domain of arccosine in (6.16) to be defined, we need

$$\left| \frac{A \pm \sqrt{A^2 + 4\tau(\tau \hat{J}_k^2 - 2v_0 A)}}{2\hat{J}_k \tau} \right| \le 1.$$

When k = 0, the minus case does not satisfy this inequality and the plus case can be rewritten as the set of conditions.  $J_0 < -2$ ,  $v_+ > 1$ , and  $4E < 4J_0 + 3J_0^2$ . Therefore the Hopf and Turing-Hopf bifurcations are both instabilities of  $v_+$ 

**6.6.** Instabilities with alpha function coupling. To identify the dispersion relation and primary instabilities of the homogeneous solution with the delayed alpha function chosen for the temporal coupling profile, we assume  $v_0 > 1$ ,  $f(v) = [v-1]_+$ and  $\hat{J}_k(t) = \frac{\hat{J}_k}{\tau^2} t e^{-t/\tau} H(t)$ . The dispersion relation (6.4) becomes

(6.18) 
$$\lambda_k (1 + \lambda_k \tau)^2 + 2v_0 (1 + \lambda_k \tau)^2 = \hat{J}_k e^{-\lambda_k D}$$

Separating the real and imaginary components of (6.18) with the assumption  $Re(\lambda_k) =$ 

(6.19a) 
$$\begin{cases} \lambda_{i,k}^2 (-2\tau - 2v_0\tau^2) = \hat{J}_k \cos(D\lambda_{i,k}) - 2v_0 \\ \lambda_{i,k} (1 + 4v_0\tau - \lambda_{i,k}^2\tau^2) = -\hat{J}_k \sin(D\lambda_{i,k}) \end{cases}$$

(6.19b) 
$$\lambda_{i,k} (1 + 4v_0 \tau - \lambda_{i,k}^2 \tau^2) = -\hat{J}_k \sin(D\lambda_{i,k})$$

When  $\lambda_{i,k} = 0$ , as in the precious cases, the saddle-node and Turing bifurcations are given by (6.7) and (6.12) respectively.

Next we identify the other two types of instabilities which have non-zero temporal frequency. From the real part of the dispersion relation (6.19a), we solve for  $\lambda_{i,k}$ 

$$\lambda_i = \pm \sqrt{\frac{\hat{J}_k \cos(\lambda_i D) - 2v_0}{-2\tau - 2v_0 \tau^2}}$$

and substitute it into the imaginary equation (6.19b), (6.20)

$$\left(\frac{\hat{J}_k \cos(\lambda_{i,k}D) - 2v_0}{-2\tau - 2v_0\tau^2}\right) \left(1 + 4v_0\tau - \left(\frac{\hat{J}_k \cos(\lambda_{i,k}D) - 2v_0}{-2\tau - 2v_0\tau^2}\right)\tau^2\right)^2 = \hat{J}_k^2 \sin^2(\lambda_{i,k}D)$$

Then, using the identity  $\sin^2 x = 1 - \cos^2 x$  and defining  $y := \cos(\lambda_{i,k}D)$ , we have the equation

(6.21) 
$$\left( \frac{\hat{J}_k y - 2v_0}{-2\tau - 2v_0 \tau^2} \right) \left( 1 + 4v_0 \tau - \left( \frac{\hat{J}_k y - 2v_0}{-2\tau - 2v_0 \tau^2} \right) \tau^2 \right)^2 = \hat{J}_k^2 (1 - y^2)$$

which can be rewritten as cubic in y

$$(6.22) - \frac{\hat{J}_k^3 \tau}{8(\tau v + 1)^3} y^3 + \frac{\hat{J}_k^2 \left(4\tau^3 v^3 + 4\tau^2 v^2 + 5\tau v + 2\right)}{4(\tau v + 1)^3} y^2 - \frac{\hat{J}_k (2\tau v + 1)^2 \left(4\tau^2 v^2 + 2\tau v + 1\right)}{2\tau (\tau v + 1)^3} y + \frac{v(2\tau v + 1)^4 - \hat{J}_k^2 \tau (\tau v + 1)^3}{\tau (\tau v + 1)^3} = 0.$$

We can explicitly solve for the roots of the cubic, one of which is always real.

Finally, substituting  $\lambda_{i,k} = \frac{1}{D} \arccos(y)$  into the real equation (6.19a) gives an implicit equation of the instability in terms of the system parameters

(6.23) 
$$(\frac{1}{D}\arccos(y))^2(-2\tau - 2v_0\tau^2) = \hat{J}_k y - 2v_0$$

This is the Hopf curve when k=0 and  $\hat{J}_k=J_0$  and a Turing-Hopf curve when k=1and  $\hat{J}_{k} = J_{1}/2$ .

- L. F. Abbott and T. B. Kepler, Model neurons: From Hodgkin-Huxley to hopfield, in Statistical Mechanics of Neural Networks, L. Garrido, ed., vol. 368, Springer Berlin Heidelberg, pp. 5–18, https://doi.org/10.1007/3540532676\_37, http://link.springer.com/10.1007/3540532676\_37 (accessed 2024-10-23).
- [2] S.-I. AMARI, Dynamics of pattern formation in lateral-inhibition type neural fields, 27, pp. 77–87, https://doi.org/10.1007/BF00337259, http://link.springer.com/10.1007/BF00337259 (accessed 2025-05-21).
- [3] D. AVITABILE, M. DESROCHES, R. VELTZ, AND M. WECHSELBERGER, Local theory for spatiotemporal canards and delayed bifurcations, SIAM Journal on Mathematical Analysis, 52 (2020), pp. 5703-5747.
- [4] R. Ben-Yishai, R. L. Bar-Or, and H. Sompolinsky, Theory of orientation tuning in visual cortex., 92, pp. 3844–3848, https://doi.org/10.1073/pnas.92.9.3844, https://www.pnas. org/doi/abs/10.1073/pnas.92.9.3844 (accessed 2025-04-07).
- P. C. Bressloff, Spatiotemporal dynamics of continuum neural fields, 45, p. 033001, https://doi.org/10.1088/1751-8113/45/3/033001, https://iopscience.iop.org/article/10. 1088/1751-8113/45/3/033001 (accessed 2024-07-04).
- P. C. Bressloff, Stochastic Neural Field Theory and the System-Size Expansion, 70, pp. 1488–1521, https://doi.org/10.1137/090756971, http://epubs.siam.org/doi/10.1137/090756971 (accessed 2025-07-06).
- [7] N. BRUNEL, Dynamics of Sparsely Connected Networks of Excitatory and Inhibitory Spiking Neurons, Journal of Computational Neuroscience, 8 (2000), pp. 183–208, https://doi.org/ 10.1023/A:1008925309027.
- [8] N. Brunel and V. Hakim, Fast Global Oscillations in Networks of Integrate-and-Fire Neurons with Low Firing Rates, Neural Computation, 11 (1999), pp. 1621–1671, https://doi.org/ 10.1162/089976699300016179.
- M. A. Buice and J. D. Cowan, Field-theoretic approach to fluctuation effects in neural networks, 75, p. 051919, https://doi.org/10.1103/PhysRevE.75.051919, https://link.aps.org/ doi/10.1103/PhysRevE.75.051919 (accessed 2025-07-06).
- [10] Á. Byrne, D. Avitabile, and S. Coombes, Next-generation neural field model: The evolution of synchrony within patterns and waves, 99, p. 012313, https://doi.org/10.1103/PhysRevE. 99.012313, https://link.aps.org/doi/10.1103/PhysRevE.99.012313 (accessed 2025-05-31).
- [11] M. Camperi and X.-J. Wang, A Model of Visuospatial Working Memory in Prefrontal Cortex: Recurrent Network and Cellular Bistability, 5, pp. 383–405, https://doi.org/10.1023/A: 1008837311948, https://doi.org/10.1023/A:1008837311948 (accessed 2025-04-07).
- [12] B. G. CARLO R. LAING, WILLIAM C. TROY AND G. B. ERMENTROUT, Multiple Bumps in a Neuronal Model of Working Memory, https://doi.org/10.1137/S0036139901389495, https://epubs.siam.org/doi/epdf/10.1137/S0036139901389495 (accessed 2025-04-07).
- [13] C. C. Chow and M. A. Buice, Path Integral Methods for Stochastic Differential Equations, 5, p. 8, https://doi.org/10.1186/s13408-015-0018-5, https://doi.org/10.1186/ s13408-015-0018-5 (accessed 2024-10-23).
- [14] S. COOMBES, P. BEIM GRABEN, R. POTTHAST, AND J. WRIGHT, Neural Fields: Theory and Applications, July 2014, https://doi.org/10.1007/978-3-642-54593-1.
- [15] R. M. CORLESS, G. H. GONNET, D. E. G. HARE, D. J. JEFFREY, AND D. E. KNUTH, On the LambertW function, 5, pp. 329–359, https://doi.org/10.1007/BF02124750, https:// doi.org/10.1007/BF02124750 (accessed 2025-07-25).
- [16] Q. CORMIER, E. TANRÉ, AND R. VELTZ, Hopf bifurcation in a Mean-Field model of spiking neurons, 26, https://doi.org/10.1214/21-EJP688, https://projecteuclid.org/journals/electronic-journal-of-probability/volume-26/issue-none/Hopf-bifurcation-in-a-Mean-Field-model-of-spiking-neurons/10.1214/21-EJP688.full (accessed 2025-07-06).
- [17] A. DE MASI, A. GALVES, E. LÖCHERBACH, AND E. PRESUTTI, Hydrodynamic Limit for Interacting Neurons, Journal of Statistical Physics, 158 (2015), pp. 866–902, https://doi.org/ 10.1007/s10955-014-1145-1.
- [18] A. Destexhe, Z. F. Mainen, T. J. Sejnowski, C. E. Koch, and I. E. Segev, *Kinetic Models of Synaptic Transmission*, in Methods in Neuronal Modeling, 2nd edition ed.
- [19] G. Dumont, J. Henry, and C. O. Tarniceriu, Oscillations in a Fully Connected Network of Leaky Integrate-and-Fire Neurons with a Poisson Spiking Mechanism, Journal of Nonlinear Science, 34 (2023), p. 18, https://doi.org/10.1007/s00332-023-09995-x.
- [20] G. Dumont and C. O. Tarniceriu, Pattern Formation in a Spiking Neural-Field of Renewal Neurons, SIAM Journal on Applied Dynamical Systems, 23 (2024), pp. 2670–2694, https://doi.org/10.1137/24M1631274.
- [21] K. ENGELBORGHS, T. LUZYANINA, AND D. ROOSE, Numerical bifurcation analysis of delay

- differential equations using DDE-BIFTOOL, ACM Trans. Math. Softw., 28 (2002), pp. 1–21, https://doi.org/10.1145/513001.513002.
- [22] G. B. ERMENTROUT AND J. D. COWAN, A mathematical theory of visual hallucination patterns, 34, pp. 137–150, https://doi.org/10.1007/BF00336965, http://link.springer.com/10.1007/BF00336965 (accessed 2024-07-25).
- [23] G. FAYE AND M. HOLZER, Modulated traveling fronts for a nonlocal Fisher-KPP equation: a dynamical systems approach, Journal of Differential Equations, 258 (2015), pp. 2257–2289.
- [24] G. FAYE AND A. SCHEEL, Center manifolds without a phase space, Transactions of the American Mathematical Society, 370 (2018), pp. 5843–5885.
- [25] W. Gerstner, Population Dynamics of Spiking Neurons: Fast Transients, Asynchronous States, and Locking, 12, pp. 43–89, https://doi.org/10.1162/089976600300015899, https://ieeexplore.ieee.org/abstract/document/6789434 (accessed 2025-08-11).
- [26] I. GINZBURG AND H. SOMPOLINSKY, Theory of correlations in stochastic neural networks, 50, pp. 3171–3191, https://doi.org/10.1103/PhysRevE.50.3171, https://link.aps.org/doi/ 10.1103/PhysRevE.50.3171 (accessed 2025-07-06).
- [27] S. GROSSBERG, Contour Enhancement, Short Term Memory, and Constancies in Reverberating Neural Networks, vol. 70, Springer Netherlands, pp. 332–378, https://doi.org/10.1007/978-94-009-7758-7\_8, http://link.springer.com/10.1007/978-94-009-7758-7\_8 (accessed 2025-07-01).
- [28] S. GROSSBERG, Learning and energy-entropy dependence in some nonlinear functionaldifferential systems, Bulletin of the American Mathematical Society, 75 (1969), pp. 1238– 1242, https://doi.org/10.1090/S0002-9904-1969-12373-6.
- [29] D. Hansel and H. Sompolinsky, 13 modeling feature selectivity in local cortical circuits, 1998.
- [30] M. HARAGUS AND G. IOOSS, Local bifurcations, center manifolds, and normal forms in infinitedimensional dynamical systems, Springer Science & Business Media, 2010.
- [31] C. Huang, D. A. Ruff, R. Pyle, R. Rosenbaum, M. R. Cohen, and B. Doiron, Circuit Models of Low-Dimensional Shared Variability in Cortical Networks, 101, pp. 337–348.e4, https://doi.org/10.1016/j.neuron.2018.11.034, https://www.cell.com/ neuron/abstract/S0896-6273(18)31043-2 (accessed 2025-07-11), https://arxiv.org/abs/ 30581012.
- [32] E. M. IZHIKEVICH, Dynamical Systems in Neuroscience the Geometry of Excitability and Bursting, MIT Press, online-ausg ed.
- [33] P.-E. Jabin, V. Schmutz, and D. Zhou, Dense networks of integrate-and-fire neurons: Spatially-extended mean-field limit of the empirical measure, https://doi.org/10.48550/ARXIV.2409.06325, https://arxiv.org/abs/2409.06325 (accessed 2025-07-06).
- [34] R. Jolivet, F. Schürmann, T. K. Berger, R. Naud, W. Gerstner, and A. Roth, The quantitative single-neuron modeling competition, 99, pp. 417–426, https://doi.org/10.1007/ s00422-008-0261-x, http://link.springer.com/10.1007/s00422-008-0261-x (accessed 2025-07-01).
- [35] C. R. LAING AND C. C. CHOW, Stationary Bumps in Networks of Spiking Neurons, 13, pp. 1473–1494, https://doi.org/10.1162/089976601750264974, https://direct.mit.edu/neco/article/13/7/1473-1494/6534 (accessed 2025-03-19).
- [36] E. Montbrió, D. Pazó, and A. Roxin, Macroscopic Description for Networks of Spiking Neurons, 5, p. 021028, https://doi.org/10.1103/PhysRevX.5.021028, https://link.aps.org/doi/10.1103/PhysRevX.5.021028 (accessed 2025-04-07).
- [37] R. NAUD, N. MARCILLE, C. CLOPATH, AND W. GERSTNER, Firing patterns in the adaptive exponential integrate-and-fire model, 99, pp. 335–347, https://doi.org/10.1007/s00422-008-0264-7, http://link.springer.com/10.1007/s00422-008-0264-7 (accessed 2025-07-06).
- [38] G. K. Ocker, Dynamics of stochastic integrate-and-fire networks, (2023), https://doi.org/10. 1103/PhysRevX.13.041047.
- [39] T. Ohira and J. D. Cowan, Master-equation approach to stochastic neurodynamics, 48, pp. 2259–2266, https://doi.org/10.1103/PhysRevE.48.2259, https://link.aps.org/doi/10.1103/PhysRevE.48.2259 (accessed 2025-07-06).
- [40] S. Paliwal, G. K. Ocker, and B. A. W. Brinkman, Metastability in networks of stochastic integrate-and-fire neurons, 111, p. 064402, https://doi.org/10.1103/PhysRevE.111.064402, https://link.aps.org/doi/10.1103/PhysRevE.111.064402 (accessed 2025-07-01).
- [41] D. J. Pinto, J. C. Brumberg, D. J. Simons, G. B. Ermentrout, and R. Traub, A quantitative population model of whisker barrels: Re-examining the Wilson-Cowan equations, 3, pp. 247–264, https://doi.org/10.1007/BF00161134, http://link.springer.com/10.1007/BF00161134 (accessed 2025-07-06).
- [42] P. ROBERT AND J. TOUBOUL, On the Dynamics of Random Neuronal Networks, 165,

- pp. 545-584, https://doi.org/10.1007/s10955-016-1622-9, http://link.springer.com/10.1007/s10955-016-1622-9 (accessed 2025-07-06).
- [43] R. ROSENBAUM AND B. DOIRON, Balanced Networks of Spiking Neurons with Spatially Dependent Recurrent Connections, 4, p. 021039, https://doi.org/10.1103/PhysRevX.4.021039, https://link.aps.org/doi/10.1103/PhysRevX.4.021039 (accessed 2024-07-25).
- [44] A. ROXIN, N. BRUNEL, AND D. HANSEL, Role of Delays in Shaping Spatiotemporal Dynamics of Neuronal Activity in Large Networks, Physical Review Letters, 94 (2005), p. 238103, https://doi.org/10.1103/PhysRevLett.94.238103.
- [45] V. SCHMUTZ, E. LÖCHERBACH, AND T. SCHWALGER, On a Finite-Size Neuronal Population Equation, 22, pp. 996–1029, https://doi.org/10.1137/21M1445041, https://epubs.siam. org/doi/10.1137/21M1445041 (accessed 2025-07-06).
- [46] T. SCHWALGER AND A. V. CHIZHOV, Mind the last spike firing rate models for mesoscopic populations of spiking neurons, Current Opinion in Neurobiology, 58 (2019), pp. 155–166, https://doi.org/10.1016/j.conb.2019.08.003.
- [47] J. SIEBER, K. ENGELBORGHS, T. LUZYANINA, G. SAMAEY, AND D. ROOSE, DDE-BIFTOOL Manual - Bifurcation analysis of delay differential equations, Sept. 2016, https://doi.org/ 10.48550/arXiv.1406.7144, https://arxiv.org/abs/1406.7144.
- [48] C. TEETER, R. IYER, V. MENON, N. GOUWENS, D. FENG, J. BERG, A. SZAFER, N. CAIN, H. ZENG, M. HAWRYLYCZ, C. KOCH, AND S. MIHALAS, Generalized leaky integrate-and-fire models classify multiple neuron types, 9, p. 709, https://doi.org/ 10.1038/s41467-017-02717-4, https://www.nature.com/articles/s41467-017-02717-4 (accessed 2025-07-01).
- [49] J. TOUBOUL AND R. BRETTE, Dynamics and bifurcations of the adaptive exponential integrateand-fire model, 99, pp. 319–334, https://doi.org/10.1007/s00422-008-0267-4, http://link. springer.com/10.1007/s00422-008-0267-4 (accessed 2025-07-06).
- [50] H. UECKER, Numerical continuation and bifurcation in Nonlinear PDEs, SIAM, 2021.
- [51] C. VAN VREESWIJK, L. F. ABBOTT, AND G. BARD ERMENTROUT, When inhibition not excitation synchronizes neural firing, Journal of Computational Neuroscience, 1 (1994), pp. 313–321, https://doi.org/10.1007/BF00961879.
- [52] A. VANDERBAUWHEDE AND G. IOOSS, Center manifold theory in infinite dimensions, in Dynamics reported: expositions in dynamical systems, Springer, 1992, pp. 125–163.
- [53] M. A. WHITTINGTON, R. D. TRAUB, N. KOPELL, B. ERMENTROUT, AND E. H. BUHL, Inhibition-based rhythms: Experimental and mathematical observations on network dynamics, International Journal of Psychophysiology, 38 (2000), pp. 315–336, https://doi.org/10.1016/S0167-8760(00)00173-2.
- [54] H. R. WILSON AND J. D. COWAN, Excitatory and Inhibitory Interactions in Localized Populations of Model Neurons, 12, pp. 1–24, https://doi.org/10.1016/S0006-3495(72)86068-5, https://linkinghub.elsevier.com/retrieve/pii/S0006349572860685 (accessed 2024-10-29).